Associating and tuning sodium and oxygen mixed-ion conduction in niobium-based perovskites

Guillaume Gouget, Fabrice Mauvy, U-chan Chung, Sébastien Fourcade, Mathieu Duttine, Marc-david Braida, Thierry Le Mercier, Alain Demourgues

Article type: Full Paper

Associating and Tuning Sodium and Oxygen Mixed-ion Conduction in Niobium-based Perovskites

*Guillaume Gouget, Fabrice Mauvy, U-Chan Chung, Sébastien Fourcade, Mathieu Duttine, Marc-David Braida, Thierry Le Mercier, and Alain Demourgues**

Dr. G. Gouget, Prof. F. Mauvy, Dr. U-C Chung, S. Fourcade, Dr. M. Duttine, Dr. A. Demourgues
CNRS, Université de Bordeaux, ICMCB, UMR 5026, 87 Avenue du Dr. Albert Schweitzer, 33608 F Pessac Cedex, France
E-mail: alain.demourgues@icmcb.cnrs.fr
Dr. M.-D. Braida, Dr. T. Le Mercier
Solvay, Research and Innovation Center Paris, F-93308, Aubervilliers, France

Keywords: niobate perovskites, oxygen conductivity, sodium conductivity, mixed ion conduction, spark plasma sintering.

Pure ionic conductors as solid-state electrolytes are of high interest for electrochemical energy storage and conversion devices. They systematically involve only one ion as the charge carrier. The association of two mobile ionic species, one positively and the other negatively charged, in a specific network should strongly influence the total ion conduction. Nb^{5+}- ($4d^0$) and Ti^{4+}-based ($3d^0$) perovskite-derived frameworks containing Na^+ and O^{2-} as mobile species are investigated as mixed ion conductors by electrochemical impedance spectroscopy. The design of Na^+ blocking layers *via* sandwiched pellets sintered by spark plasma sintering (SPS) at high temperatures leads to quantified transport of both ionic charge carriers t_{Na+} and t_{O2-}. In the 350-700 °C temperature range, ionic conductivity can be tuned from a majority Na^+ contribution (t_{Na+} = 88 %) for $NaNbO_3$ to pure O^{2-} transport in the $NaNb_{0.9}Ti_{0.1}O_{2.95}$ phase. The Ti-substitution is accompanied with an approximately 100-fold increase in the oxygen conductivity, which approaches the best values for pure oxygen conductors in this temperature range. Conduction evolutions are correlated to the composition and structural features of the distorted perovskite networks in terms of distortions of polyhedra and vacancy management through mixed valence states. In addition to the demonstration of tunable mixed ion conduction

with quantifiable cationic and anionic contributions in a single solid-state structure, a strategy is established from structural analysis to develop other architectures with improved mixed ionic conductivity.

1. Introduction

Electrochemical energy storage and conversion devices such as batteries or fuel cells rely on the design of electrode materials with mixed ion/electron conduction and solid electrolytes with high ionic conductivity.[1–5] These properties are strongly dependent on the chemical composition, the solid network architecture and, at the atomic scale, the chemical bonding; which has direct implications on the electronic band diagram, as well as chemical or electrochemical potential for electrons at the Fermi level.[6,7] Such considerations are of great interest to assess the anionic redox processes which occur at the cathode in Li-ion batteries, and their interplay with cationic electrochemistry.[8–10] In all solid-state batteries, research focus is primarly dedicated to electrolytes. LISICON materials are lithium super ionic conductors (Li/Al/Ti-based phosphates, $\sigma = 10^{-3}$ S.cm^{-1} at room temperature-RT) which adopt a 3D ribbon network where Li^+ ions are located in interstitial sites. However, they are electrochemically unstable against Li-metal.[11] Li garnet ($Li_7La_3Zr_2O_{12}$), which also exhibits a 3D framework, is a promising type of electrolyte for Li-metal batteries due to its high lithium-ion conductivity ($\sigma = 10^{-4}$ to 10^{-3} S.cm^{-1} at RT) and better electrochemical stability against lithium-metal.[12,13]

Sodium is a second alkali metal that has a larger ionic size than lithium, and is a low-cost and naturally abundant alternative to lithium.[14–17] However, replacing sodium for lithium will require a lot of improvement from a materials perspective to achieve competing performances. High Na^+ ionic conductivity can be achieved with NASICON (Na^+ super ionic conductor, Na/Zr/Si-based phosphates with $\sigma \approx 10^{-4}$ S.cm^{-1}) which also exhibit a 3D ribbon structure where Na^+ ions occupy interstitial sites.[18,19] In the last few years, efforts on novel electrode and electrolyte materials successfully yielded room-temperature battery devices.[20,21] A new

NASICON (Na/Zr/Mg-based silicate-phosphate) has been shown to exhibit high room-temperature ionic conductivity ($\sigma = 3.5 \times 10^{-3}$ S.cm^{-1}).[22] However, most commercially developed sodium-based accumulators rely on a sodium-sulphur electrochemical cell operated around 320 °C with liquid Na and liquid S as positive and negative electrodes, respectively. The electrodes are separated by β-alumina (Na_2O-$11Al_2O_3$) as solid electrolyte.[23,24] During the discharge, Na^+ formed at the anode migrates along the electrolyte to the cathode and forms liquid sodium polysulfides. The network of β-alumina is bidimensionnal (intergrowth of spinel blocks and the conduction layer which are alternately stacked) in which Na^+ ions occupy the loosely packed NaO plane. Na^+ ionic conductivity in β-alumina single crystals with excess Na decreases from 15 S.cm^{-1} at T = 350 °C to 1.4×10^{-2} S.cm^{-1} at RT.[25] In polycrystalline undoped ceramics, it drops to 5.6×10^{-2} S.cm^{-1} at 350 °C.[26] Despite competing energy and power densities,[27] Na-S battery technology remains limited to niche applications, due to liquid sodium polysulfide reactivity that causes hazardous issues and a drop in electromotive force along the discharge.

Based on the same concept as sodium-sulphur batteries, an original sodium-air electrochemical cell can be proposed by replacing the sulfur species by their oxygen counterpart. In such a case, the reduction of oxygen gas ($1/2\ O_2 + 2\ e^- \rightarrow O^{2-}$) at the cathode (e.g. Ag electrode) and oxidation of liquid-Na at the anode ($2\ Na \rightarrow 2\ Na^+ + 2\ e^-$) should take place during the electrochemical process, leading to the formation of Na_2O. The theoretical electromotive force or the potential difference is related to the free energy ΔG of Na_2O binary oxide corresponding to ΔE = 1.93 V (under Open Circuit Voltage conditions).[28] In this concept, sodium and/or oxygen ion conductors can be used as solid electrolytes. This leads to three questions: (i) Is it possible to design mixed Na^+ and O^{2-} ion conductors in order to enhance the global ionic mobility for this application, with a synergy between sodium and oxygen migration in a single framework? (ii) What kind of interactions arise between Na^+- and O^2-sub-networks with various

ionic polarizabilities and potential synergic effects involved?(iii) Can we determine both contributions to the total ion conduction through calculation of the ionic transport numbers of each carriers?

In the solid-state chemistry approach, ionic transport associated to ionic diffusion into solids is described by the hopping of ionic species (Li^+, Na^+ or O^{2-}) from one lattice site to an adjacent one through inter-connected diffusion paths in the framework.[29–31] Each hopping mechanism is associated with energy barriers. High concentration of mobile ion carriers (vacancies or interstices), large mobility, and a low activation energy are required to achieve high ionic conductivity. Among solid-state electrolytes in solid oxide fuel cells (SOFC), 8 $\%_{mol.}$ yttria stabilized zirconia (YSZ-8), 10 % gadolinium-substituted ceria (CGO), and bismuth oxide display exclusive O^{2-} conductivity of ca. 10^{-4} to 10^{-3} $S.cm^{-1}$ at 400 °C.[32–34] Their network is derived from the fluorite-type structure favoring the stabilization of oxygen vacancies. The conductivity of these state-of-the-art oxygen conductors remains lower than the Na^+ conductivity in NASICON or β-alumina in the same temperature range.[19,26] O-deficient perovskites (general formula ABO_3) stand amongst the best O^{2-} ionic conductors at relatively low temperatures ($NaNb_{0.5}Al_{0.5}O_{2.5}$, $NaTa_{0.5}Al_{0.5}O_{2.5}$, $Na_{0.5}Bi_{0.49}TiO_{2.985}$ and $Ba_3MoNbO_{8.5}$), with conductivity varying between 5×10^{-5} and 5×10^{-4} $S.cm^{-1}$ at T = 400°C.[35–38] The activation energies are 0.7-1 eV for O-deficient fluorite-type networks, compared to 0.4-0.5 eV for the perovskite-derived phases mentioned above. This is comparatively higher than values of 0.2 to 0.3 eV reported for Na^+-conductive β-alumina.[22,25,26] However, in the case of perovskite-derived networks, the ambiguity is maintained on the assignement of the mobile carrier through calculation of activation energy. For instance, A-site defective $Na_{3x}La_{1.33-x}\square_{0.67-2x}Ti_2O_6$ ($x \leq 0.28$) are sodium conductors with a higher activation energy of 0.92 eV, and independent on x due to the energetic barrier associated with the hopping mechanism of sodium cations.[39] In perovskite-derived structures with both Na^+ and O^{2-} potential conduction, activation energy measurements thus do not enable concluding on the nature of conduction carriers.

Several recent discoveries highlight perovskite-derived structures as efficient oxygen ion conductors below 700 °C, paving the way towards relatively low temperature applications.[36,38] Titanates and niobates with perovskite structures have been widely investigated due to the occurrence of polar phases associated with piezoelectric[40–43] and ferroelectric[44–47] properties, as well as a rich polymorphism versus temperature.[48–53] This structural complexity extends at room temperature for $NaNb_{1-x}Ti_xO_{3-0.5x}$ ($0 \leq x \leq 0.20$), with the occurrence of two structures, where only one of them is polar and crystallizes in the acentric $P2_1ma$ space group.[54–57] Both the inequivalent Na sites are close in energy and stability in $P2_1ma$ network, whereas they are radically different in the centrosymmetric structure (Pbma space group). Nb^{5+} ($4d^0$) and Ti^{4+} ($3d^0$) are stabilized in such perovskite networks and exhibit second-order Jahn-Teller distortion (SOJT), which arises from octahedral deformation due to high ionic charge, small ionic size (high polarizing power), and a relatively low bandgap (3.5 eV) involving the mixing p(O) and d(Nb, Ti) orbitals. For $NaNbO_3$, the SOJT distortion of Nb^{5+} ($4d^0$) is exhibited in the $P2_1ma$ network where the two Na atoms sites share the same symmetry operators, which is not the case for Pbma space group. Na sites constrain [NbO_6] octahedron to be more distorted but less rigid in the $P2_1ma$ framework by competitive bonds. Such distortions favor oxygen mobility.[56] $NaNb_{1-x}Ti_xO_{3-0.5x}$ ($0 < x \leq 0.20$) complex oxides were very recently shown to preferentially crystallize in the low-temperature form of sodium niobate in the acentric $P2_1ma$ space group.[57] More specifically, the ionic conductivity in $NaNb_{0.85}Ti_{0.15}O_{2.925}$ varies between 3×10^{-5} and 2×10^{-3} $S.cm^{-1}$ in the studied interval $300 < T < 700$ °C. Such performances compete with YSZ-8 ($\sigma = 10^{-4}$ $S.cm^{-1}$ at 400 °C) and CGO ($\sigma = 3.10^{-4}$ $S.cm^{-1}$ at 400 °C).[32] This is also one to two orders of magnitude higher than the conductivity in $NaNbO_3$.

However, in this titanium-substituted sodium niobate series, the nature of the mobile species remains unclear, as Na^+ and O^{2-} could potentially contribute to the ionic conductivity mechanism. The activation energy slightly increases from 0.51 to 0.61 eV with Ti content from 5 to 15 %.[57] This can be naturally correlated to the increase of oxygen vacancy rate as well as

the crystal-field (SOJT) stabilization energy around Nb^{5+}/Ti^{4+} centers, yielding facilitated O mobility. The concentration of O^{2-} carriers is directly linked to O^{2-} vacancies, whereas their mobility is limited by the hopping between two oxygen sites with an energy barrier for ionic diffusion. The creation of O^{2-} vacancies is associated with the decrease of Nb(Ti)-O bond lengths and the Nb(Ti)-O orbital overlapping. Thecovalence should then slightly increase, which explains the increase in activation energy. Despite this convincing argument, the unlikely but potential contribution of Na^+ must be assessed. In this sodium niobate series, the contribution of each Na^+ and O^{2-} mobile ions carriers (e.g. their ionic transport number) must first be quantified, then discussed with respect to the general perovskite-type structural family. This is necessary to finally draw structural requirements in order to efficiently associate Na^+ and O^{2-} ions mobilities in optimized solid electrolytes with improved and balanced ionic conductivity.

The starting point to address these issues is the original design of Na^+ blocking and O^{2-} conducting solid electrolyte sandwiched electrochemical cells formed during a single Spark Plasma Sintering (SPS) step. This strategy has already been proven successful in the case of monolithic Li-ion batteries.[58] Prior to that, the stabilization of Nb^{4+} and oxygen vacancies in sodium niobate was observed after SPS at high temperatures (from 900°C to 1200°C) under reducing atmosphere. Conductivity measurement versus temperature under an argon environment highlights a switch from electronic conductivity (Nb^{4+}) at low temperature to ionic conductivity at temperatures close to 550-600 °C. Niobium oxidation occurs concommintantly to deep structural reorganization characterized by the strong polymorphism of $NaNbO_3$ in this temperature range. Complex impedance diagrams on ceramics with Na^+-blocking layers allow the determination of the exclusive O^{2-} bulk contributions to conductivity in sodium niobates and sodium titanates-niobates. The strong variability of Na^+ and O^{2-} relative contributions is demonstrated in a single framework type upon Ti substitution, paving the way toward mixed conductors with finely tuned contributions of both ionic carriers. On the basis of this

unprecedented discovery, a strategy is defined towards complex oxides with enhanced mixed Na^+/O^{2-} ionic conductivity.

2. Results

2.1. Composition and total conductivity of dense ceramics of sodium niobate

$NaNbO_3$ ceramics with a relative density of at least 94 % are achieved by SPS. After this treatment, the network remains identical with the Pbma space group (**Figure 1**a, see also **Table S1**), as confirmed by a typical signature in the region $35.5\ ° < 2\Theta < 44.5\ °$ (Cu K_α source).[45,51,55–57] Despite the similarities of X-Ray diffraction (XRD) patterns of both RT polymorphs, the NbO_6 octahedron distortion and complex octahedral tilt schemes vary in connection with Na local environments (**Figure 1b**). The closest Nb-O bond lengths involving the two apical oxygens (O1 and O2 in the vicinity of Na1 and Na2 respectively, **Figure 1b**) and the alternation of longer and shorter Nb-O bond distances in the equatorial plane (O3 and O4), underline the octahedral tilts schemes in three different directions, as well as the key role of Na atomic positions which indirectly influence the second order Jahn-Teller distortion. As opposed to the acentric polymorph, the centrosymmetric structure in the Pbma space group displays distinct Na atomic sites by means of environnemnt (symmetry, Na-O lengths) and stability, contributing to a less distorted but more rigid framework.[56]

After the SPS treatment, the structure is maintained, but the color of the pellet turns to blue-gray, while the powder is initially white. The UV-visible spectrum in **Figure 1c** displays a strong absorption in the visible range, which is the signature of n-type semiconducting behavior. The electron spin resonance (ESR) spectrum represented on **Figure 1c** reveals a broad signal associated with the paramagnetic species in an anisotropic environment with an average g value of ~1.95, attributed to the occurrence of the Nb^{4+} ($4d^1$) Jahn-Teller ion stabilized in an elongated octahedral site. In comparing sodium niobates before and after SPS treatment using ^{93}Nb NMR spectra (**Figure 1d**), a strong Knight shift is observed. This shift is attributed to electron conduction in a semiconductor, definitively confirming the presence of Nb^{4+} stabilized

in sodium niobate after SPS at T = 900 °C. Moreover, after annealing of the SPS-treated pellet under air at 900 °C, the sodium niobate turns to white and crystallizes in the Pbma structure (**Figure S1**). It is noteworthy that a SPS treatment at higher temperatures (T = 1200 °C) affects the unit cell parameters with a global increase of the unit cell volume due to the stabilization of a larger content of Nb^{4+} ions (**Figure S2**).

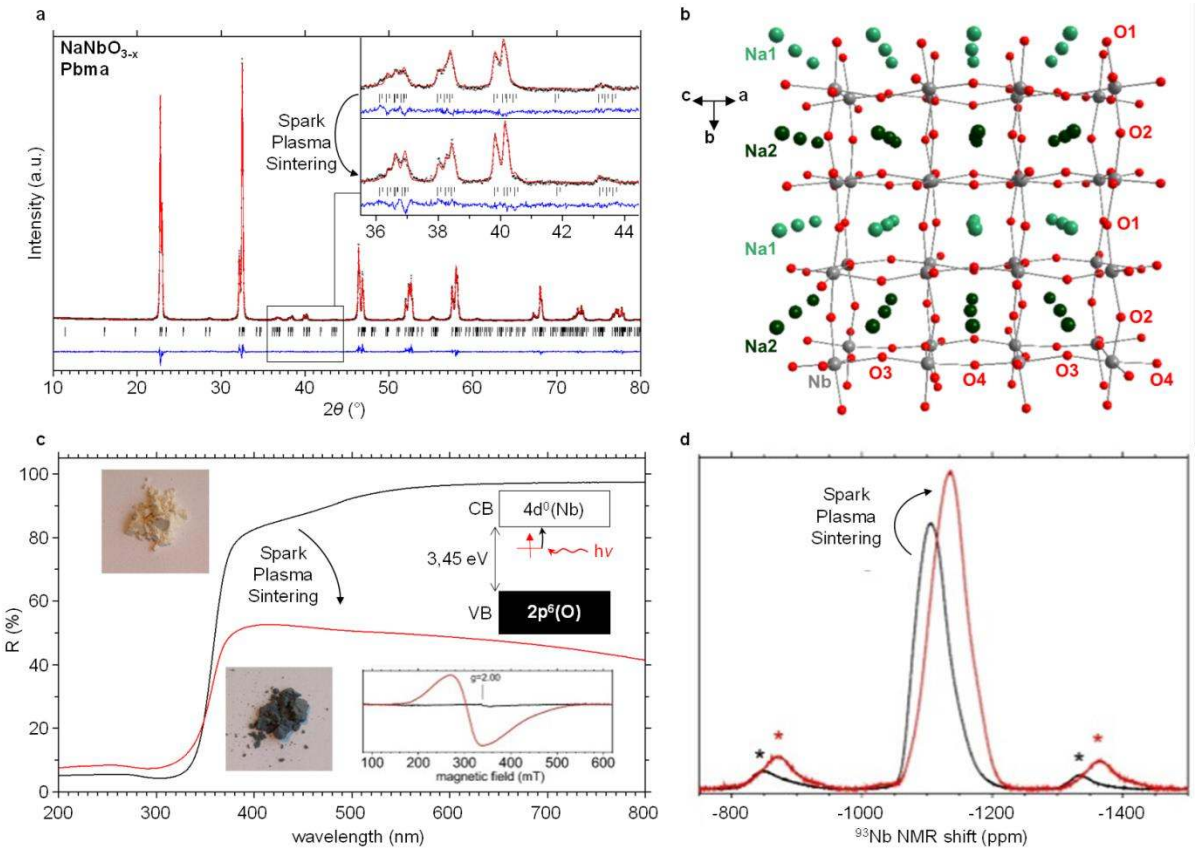

Figure 1. $NaNbO_{3-x}$ obtained from Spark Plasma Sintering. a) XRD Rietveld refinement of in the Pbma space group after SPS at 900 °C during 5 min. The zoom in the region $35.5 \leq 2\theta \leq 44.5$ ° highlights the stability of the structure versus the acentric polymorph ($P2_1ma$ space group). b) Structure of $NaNbO_3$ in the Pbma space group, c) diffuse reflectance of initial $NaNbO_3$ (white powder) and powdered pellet from SPS (gray-blue powder). Insets: (lower) room temperature X-band ESR spectra of sodium niobate before and after SPS showing strong Nb^{IV} coupling and (upper) band diagram of $NaNbO_{3-x}$ typical of n-type semi-conductors. Free electrons in the forbidden band are promoted in the conduction band (CB) through absorption in the visible range. VB: valence band. d) ^{93}Nb MAS NMR spectra of sodium niobate before and after sintering (* spinning sidebands, MAS rate: 30 kHz).

In order to better understand the thermal evolution of the partially reduced sodium niobate conductivity under neutral gas, phase transitions have been evidenced in a first step by X-ray diffraction in the same temperature range (**Figure 2**a and b). Two different orthorhombic space

groups (Pbmn and Cmcm) and one tetragonal (P4/mbm) are identified as the reduced unit cell parameter of the perovskite network a_{cub} deviates from the linear thermal expansion. The change of symmetry is directly connected to the NbO_6 octahedron tilt scheme and distortion also associated with the Na atomic position and related polarizabilities. Overall, five of the six major polymorphs of $NaNbO_3$ above RT are identified from the reduced sample, at expected temperatures. It is noteworthy that the color of the powder ceramic evolves from blue-grey to white (**Figure 2a**) after the sample cooled down to room temperature under helium atmosphere. The thermal variation of the conductivity under argon up to T = 900 °C (**Figure 2b**) shows two distinct behaviors with two radically different associated activation energies: 0.14 eV with $\sigma = 10^{-4}$ S.cm^{-1} at T = 200°C during the initial raise in temperature, and 0.83 eV above 600 °C and then during the decrease of T, with $\sigma = 2\times10^{-8}$ S.cm^{-1} at T = 200 °C in the final stage of the experiment (data from complex impedance spectroscopy). In the first step, from RT to around 550 °C, the n-type conductivity is attributed to promoted d electrons coming from Nb^{4+} stabilized in sodium niobates. At temperatures around 550-600°C, several phenomena occur concommitently: (i) Nb^{4+} oxidizes into Nb^{5+} under low oxygen partial pressure (2×10^{-5} atm) of argon or helium atmosphere, as observed by the recovery of a white color, (ii) the conductivity at 600 °C is lower than at 550 °C as a consequence of the loss of electron charge carriers, (iii) ion conduction takes over, as confirmed by the following high activation energy of 0.83 eV, and (iv) major structural rearrangements of the distorted perovskite framework take place (**Figure 2**d); specifically the transition from the orthorhombic Cmcm to the tetragonal P4/mbm space group, which is accompanied with the decrease of O distinct sites from 3 to 2 and Na distinct sites from 2 to 1. Following the increase of temperature above the critical temperature (550-600 °C) under argon, the conductivity measured under air from T = 900 °C to RT(e.g. without any O-vacancy maintained in the structure) indicates a similar slope in the Arrhenius plot, corresponding to $E_a = 0.83$ eV. As a consequence, Na^+ is the sole charge carrier in the oxidized structure. This key feature will be further discussed. SPS sintering is shown to yield

partially reduced niobates with a conductive behavior associated with electron carriers. However, heat treatment above a critical temperature and at relatively low oxygen partial pressures allows the recovery of a fully oxidized material with exclusive ion conduction.

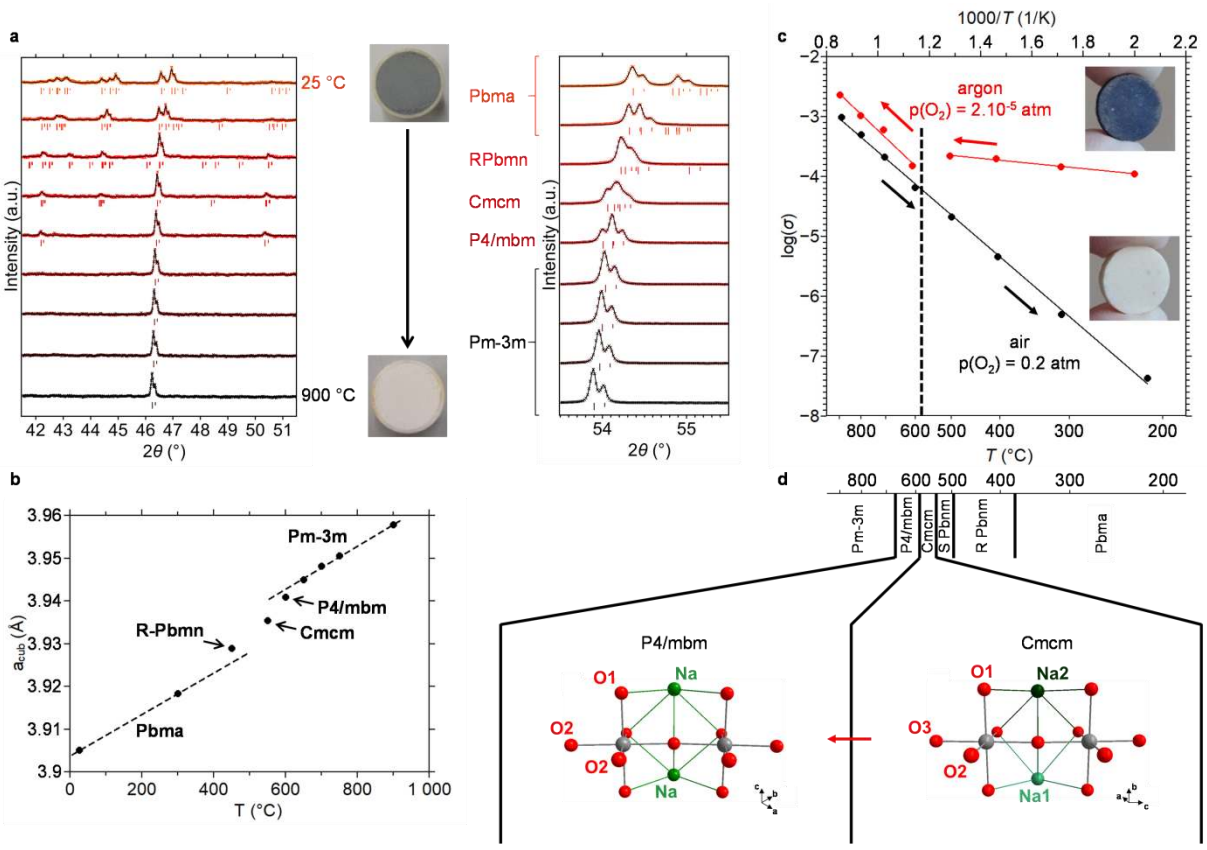

Figure 2. Switch in conduction mode of sodium niobate driven by phase transition. a) Structural transitions and parallel oxidation of $NaNbO_{3-x}$ with temperature under helium. Note the Co $K_\alpha1/K_\alpha2$ X-ray source used here (λ = 1.7890/1.7919 Å). Reflection positions were calculated from Rietveld refinements (black curves) of XRD patterns (orange to black crosses). The color of the powder evolves from gray-blue before the experiment to white, as observed after the sample cooled down to RT in helium atmosphere. b) Deviation of reduced cell parameter to linear dependence with temperature due to phase transition. c) Switch from electronic to ionic conductivity and parallel oxidation of $NaNbO_{3-x}$ with temperature. Starting with the blue pellet, the conductivity was measured under argon for increasing *T* and under air for decreasing *T*. After the experiment, the pellet has turned white. Data from complex impedance spectroscopy. d) Reported phase transitions of $NaNbO_3$ with temperature[51] and structural rearrangements during quadratic transition occurring in parallel to $NaNbO_{3-x}$ reoxidation.

2.2. Blocking layer method

In the case of sodium (titanate) niobates, ionic conductivity can be attributed to the displacement of either Na^+, O^{2-} or both ions in the perovskite lattice. In this case, one of the key characterstics is to determine the specific transport number of these ions depending on the

structure and the chemical compositions. The transport number of a mobile charged species quantifies the contribution of each carrier to the transport of current in the solid. It is defined by **Equation 1**:

$$\boldsymbol{t_i = \frac{\sigma_i}{\sigma_{tot}}} \quad \textbf{(1)}$$

where t_i is the transport number of the carrier type i, σ_i is the conductivity of the species i and σ_{total} is the total conductivity of the solid.

In the solid-state electrochemistry approach, different methods exist to estimate the transport number of charge carriers. Excluding the isotopic exchange methods,[59] most of them are applications of Wagner's theory.[60] The following main approaches can be mentioned: the concentration cell method, the mass balance approach, the semi-permeability flow method,[61] the conductivity relaxation method[62,63] and the Coulometric techniques. According to Wagner, the steady oxygen permeation flux density controlled by bulk diffusion in a mixed conductor is given by **Equation 2**:

$$J_{O_2} = \frac{RT}{16.F^2.L} \int_{P_{O_2}^{lean}}^{P_{O_2}^{rich}} \frac{\sigma_i.\sigma_e}{\sigma_i+\sigma_e}.c \ln P_{O_2} \quad (2)$$

where all the symbols have their original meaning and L is the sample membrane thickness.

In most cases, these methods have been used for materials whose charge carriers are mainly oxygen ions, and more rarely cations. An oxygen activity gradient is necessary and two gas tight compartiments are required to induce an electromotive force (e.m.f. method), or to it is necessary to generate an ionic flow through the dense ceramic sample (semi-permeability flow method). Using these approaches, the determination of the transport numbers is not accurate. The plateau or inflection points are very difficult to highlight on the chronoamperometry curves when the ionic conduction properties are closed due to the difficulty to maintain both sides perfectly sealed at high temperature.[64] Otherwise, the sample has to be perfectly stable under the activity gradient. This is the reason why the blocking layer method has been selected in the present work.

For this purpose, Yttria Stabilized Zirconia with 8 % of Y_2O_3 (YSZ-8) has been selected. It is considered as a pure O^{2-} ionic conductor. This material has a transport number t_{O2-} very close to 1 under air and in the temperature range (RT < T < 900 °C) with a low number of electronic transport t_{e-} < 0.001. It is noteworthy that the diffusion of the alkaline cations is close to zero in the zirconia material which can be considered as blocking layer for the diffusion of Na^+.

In the present work, the specific ion conduction of O^{2-} is determined for two representative compositions of the $NaNb_{1-x}Ti_xO_{3-0.5x}$ complex oxides series: x = 0 and 0.10. Symmetrical sandwich-type samples YSZ-8/$NaNb_{1-x}Ti_xO_{3-0.5x}$/YSZ-8 are sintered in a single step by the SPS method at 1100 °C. As previously mentioned, $NaNbO_3$ sintered by SPS at T = 1200 °C still adopts the structure in the Pbma space group despite a large content of Nb^{4+} ions (**Figure S2**). An additionnal heat treatment is then performed at 800 °C during 12 h under air, reoxidizing the Nb^{4+} centers into Nb^{5+}. The reactivity between the niobate materials and YSZ-8 upon SPS followed by annealing under air is assessed by XRD. As depicted in **Figure S3**, no additional phase appears upon the thermal treatment. A scanning electron microscope (SEM) image of typical sandwich-type samples containing $NaNbO_3$ and $NaNb_{0.9}Ti_{0.1}O_{2.95}$ are represented by **Figure 3**a and **Figure S4**, respectively. The three different layers can be clearly distinguished. SEM images help to confirm the high density and homogeneity of the YSZ-8 and $NaNb_{1-x}Ti_xO_{3-0.5x}$ parts (**Figure 3b** and **Figure S4**). Additionally, the interfacial regions between the different layers display well-defined compositional frontiers, as observed by energy dispersive X-Ray mapping, thus confirming the absence of elemental diffusion from one part to another. Finally, homogeneous interfacial regions are observed, thus facilitating O^{2-} ionic transfer. In this sandwich-type architecture, only the oxygen ions can be exchanged with YSZ-8 and the Na^+ ion conduction is blocked (see **Figure 3c** and **Figure S4**). Electrochemical Impedance Spectroscopy (EIS) is then performed on these ceramic samples.

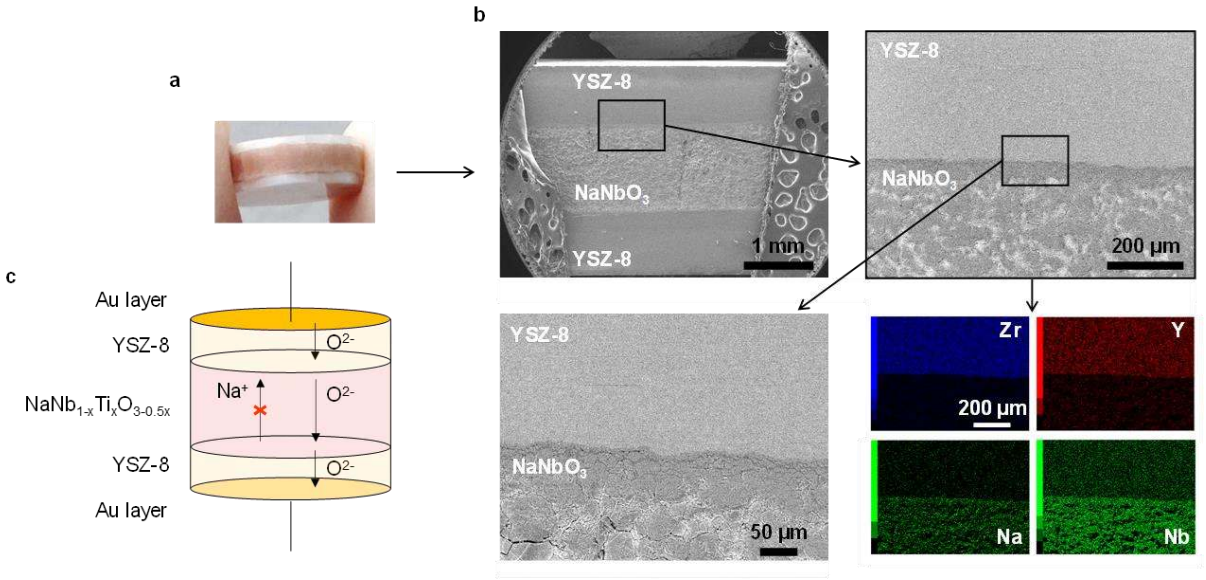

Figure 3. Na^+ blocking- O^{2-} conducting- YSZ-8 solid electrolyte sandwiching $NaNb_{1-x}Ti_xO_{3-0.5x}$ (x = 0, 0.10). a) YSZ-8/$NaNbO_3$/YSZ-8 sandwiched pellet (D x e = 10,00 x 3,07 mm^2) after SPS followed by annealing under air, b) SEM images and EDX mapping at the YSZ-8/$NaNbO_3$ interface. Cross-section view of the sandwiched pellet. c) Symmetrical system used for complex impedance spectroscopy. Electrodes consist of Au thin layer deposited on YSZ-8 by ion sputtering. YSZ-8 electrolytes prevent from Na^+ conduction in $NaNb_{1-x}Ti_xO_{3-0.5x}$ (x = 0, 0.10). In sandwiched pellets, O^{2-} is the only effective charge carrier.

2.3. Electrochemical Impedance Spectroscopy (EIS)

The impedance diagrams were measured in the 200-800 °C temperature range under air, using symmetrical cells. Under steady-state conditions, the diagrams show several contributions, as exemplified in **Figure 4**. Some of the depressed semi-circles are assigned to the intrinsic properties of the materials, and the others to phenomena occurring at the mixed Na^+/O^{2-} ionic conductor ($NaNb_{1-x}Ti_xO_{3-0.5x}$)/YSZ-8, or at the YSZ-8/noble metal (Au) interfaces. For a specific cell made of given materials, there are different approaches to assign these impedance contributions: either by varying the geometrical factor of the ceramic sample, as it influences the measured resistances and capacitances, or by changing the operating oxygen partial pressure. In the case of YSZ-8, its well-known conduction properties do not significantly depend on the oxygen partial pressure (in the T range RT-1000 °C and P_{O2} range $1\text{-}10^{-20}$ bar), while the interface polarizations (electrode reaction) are strongly affected.[65] At constant temperature and oxygen partial pressure, the impedance contributions of all the carriers are simultaneously

measured in the frequency space and very difficult to deconvolute without reference samples. Consequently, EIS measurements on Au/YSZ-8/Au and Au/$NaNb_{1-x}Ti_xO_{3-0.5x}$/Au samples referred to as single-phase cells are compared to results from sandwich-type cells, allowing identification and assignment of most contributions. All EIS diagrams recorded at various temperatures between 200 and 800 °C under air are reported on **Figure S5** and **S6**.

A typical example of Nyquist plots measured at 275 °C for $NaNb_{0.9}Ti_{0.1}O_{2.95}$ pellet with symmetrical YSZ-8 blocking layers is reported on **Figure 4**. Experimental data has been fitted on the basis of an equivalent circuit constituted of Resistance-Constant Phase Element (R-CPE) elements in parallel associated in series. Each R and CPE can be assigned to the resistance and capacitance associated to a specific electrochemical process. Usually one or two arcs more or less overlapp in the high frequency (HF) range (10^6–10^4 Hz) and in the medium frequency (MF) range (10^4–1 Hz). In the lower frequency (LF) range (1–0.01 Hz), the electrode reaction occurs (Au/air interface) and is modeled using the Warburg-type impedance. In the present study, our attention is focused on the HF and MF contributions where the studied material behavior is observed. On the basis of the fitted data, the conductivity σ, the relaxation frequency f_{relax} and the associated capacitive effect C_{eq} of each HF and MF contributions are deduced using **Equation 3**, **4** and **5**:

$$\boldsymbol{\sigma = \frac{1}{R}.\frac{l}{S}} \quad (3)$$

$$\boldsymbol{f_{relax} = \frac{1}{2\pi\,(R.CPE)^{\frac{1}{n}}}} \quad (4)$$

$$\boldsymbol{C_{eq} = R^{\frac{1-n}{n}}.CPE^{\frac{1}{n}}} \quad (5)$$

where f_{relax} , R and C_{eq} are the frequency relaxation, the resistance and the equivalent capacitive effect, respectively. l and S are the thickness and the surface of the pellet samples. CPE represents the modulus of the Constant Phase Element and n the depression parameter.

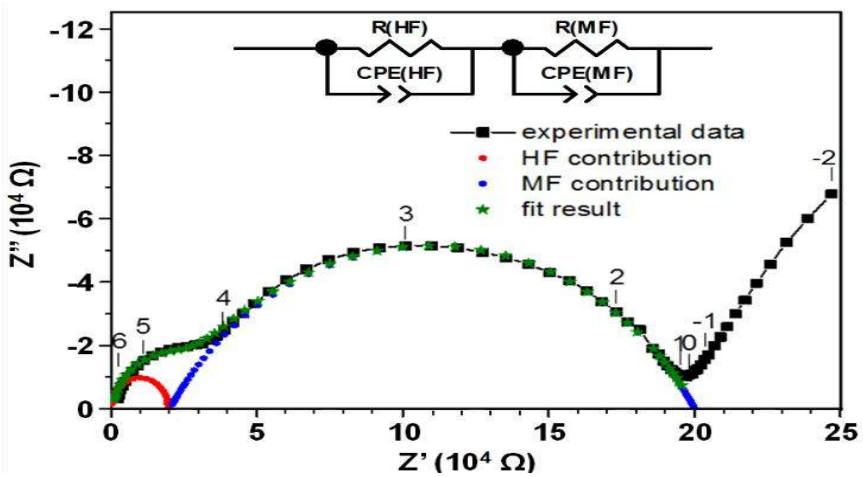

Figure 4. Typical impedance diagram obtained at 275 °C for $NaNb_{0.9}Ti_{0.1}O_{2.95}$ with symmetrical YSZ-8 blocking layers (the numbers reported in the figure are the frequency logarithms).

The impedance spectra of the five samples (YSZ-8, $NaNbO_3$, $NaNb_{0.9}Ti_{0.1}O_{2.95}$ and sandwich pellets) are provided in **Figure S5** and **S6**, for temperatures ranging between 200 and 650 °C. A comparison of the fitted parameters (C_{eq}, F_{relax} and σ calculated from R) and the dimensions of samples are provided in **Table S2**, at approx. 324 °C for $NaNbO_3$-related samples and 275 °C for $NaNb_{0.9}Ti_{0.1}O_{2.95}$-related ones. The fitted parameters obtained at various temperatures are also reported on **Table S3** and **S4**. Concerning the YSZ-8 sample sintered using SPS method, only one HF semi-circle is observed. According to the equivalent capacity and the relaxation frequency, it can be concluded that the electrochemical behaviour of this ceramic sample is in good agreement with similar data reported in the literature for YSZ-8. In addition, the relative dielectric permittivity (ε_R = 23) deduced from the equivalent capacity at room temperature is also close to the value reported in the literature at room temperature (ε_R = 30).[66,67] The lower value observed with the SPS sintered sample can be assigned to dielectric losses due to the reducing condition of the SPS process. Furthermore, as the temperature increases, the YSZ-8 ceramic cannot be considered as a pure capacitor anymore as the temperature increases, because of the oxygen ion mobility. The classical RC equivalent circuit used for dielectric material is not efficient in this case. Finally, the HF arc can be assigned to the bulk conductivity of the YSZ-8.

Concerning single phase samples, the direct assignement of the Na^+ and O^{2-} conductivitiy from fitted parameters is not possible. At 325 °C, the conductivity on $NaNbO_3$, is 50 times lower than in YSZ-8. Similarly, only one depressed semi-circle is observed for the $NaNb_{0.9}Ti_{0.1}O_{2.95}$. The C_{eq} and relaxation frequencies f_{relax} are closer to YSZ-8. However, slightly higher C_{eq} and f_{relax} values account for lower conductivity ($\sigma = 2.65 \times 10^{-6}$ S.cm^{-1} at 275 °C).

Intrepretation of impedance spectra for YSZ-8/$NaNbO_3$/YSZ-8 is straightforward, as the contributions of each material occur in significantly different frequency regimes. Especially, the contribution of YSZ-8 bulk conductivity is not observed anymore at 415 °C and above (**Figure S5**). For the YSZ-8/$NaNb_{0.9}Ti_{0.1}O_{2.95}$/YSZ-8 sample, the two main impedance contributions are observed. In the HF range, the impedance data can be assigned to oxygen ion conductivity through the YSZ-8 layer. Indeed, both the capacitive effect and the relaxation frequency are very similar to the pure YSZ-8 contributions. Because Na^+ is blockedby the YSZ-8 layer, the MF contribution is attributed to the O^{2-} ion displacement through the $NaNb_{0.9}Ti_{0.1}O_{2.95}$ mixed conductor.

To assist the interpretation of the electrochemical data of the cells, the plots of the relaxation frequencies (f_{relax}) and equivalent capacitances (C_{eq}) of each relevant impedance contribution as a function of the reverse of the temperature are represented in **Figure 5**a and b, respectively (Arrhenius plots). The graphs display only selected contributions of each experimental impedance diagram for the sake of clarity, and can be considered a reference for interpreting a given experimental impedance diagram.[68–70] The relaxation frequency (f_{relax}) is particularly interesting as it does not depend on geometric factors, and therefore it can be directly compared from one sample to another. Resistances are also plotted as a function of the reverse of the temperature (**Figure 5c**).

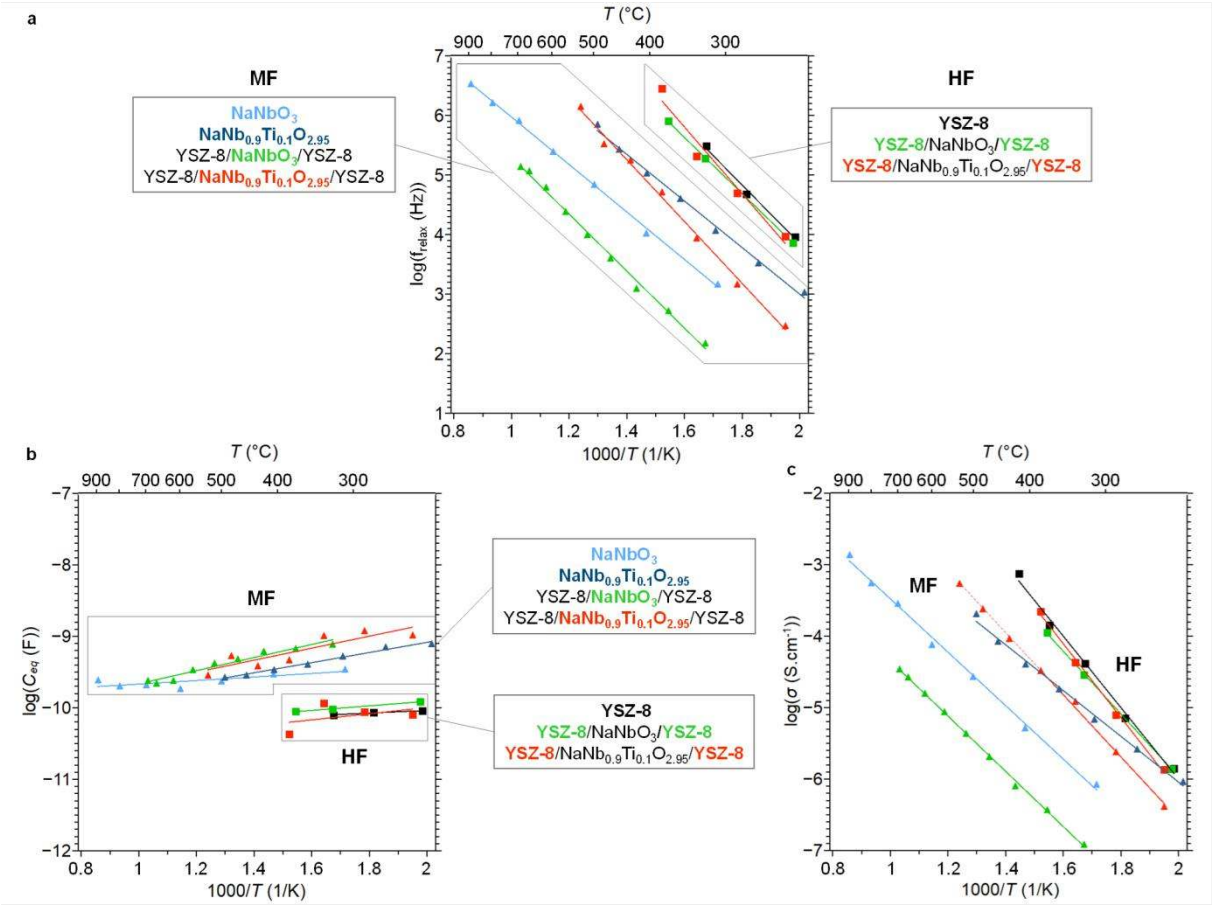

Figure 5. a) Arrhenius plots of the HF and MF relaxation frequencies for the different impedance contributions, b) associated HF and MF capacitive effects and c) Arrhenius plots of the conductivities of single phase pellets YSZ-8 and $NaNb_{1-x}Ti_xO_{3-0.5x}$ (x = 0, 0.10) and sandwich-type pellets. Contributions from YSZ-8 (squares) and $NaNb_{1-x}Ti_xO_{3-0.5x}$ (triangles) are distinguished from the thermal evolution of equivalent capacities and frequencies plots.

The results obtained for the Au/YSZ-8/Au cell obtained here are in agreement with previous works.[32] In the temperature range T > 320 °C, only one high frequency (HF) semi-circle can be observed. This impedance contribution has been assigned to the bulk conductivity of the YSZ-8 solid electrolyte. The associated equivalent capacitive effect (C_{eq}) is stable in the working temperature range and lower than 10^{-10} F. This value is very close to values reported in the literature for YSZ-8 materials. In the lower temperature range T < 320 °C, two depressed semi-circles could be observed. In that case, the arcs can be assigned to the bulk (HF) and grain boundary (MF) conductivities of the YSZ-8 electrolyte. Using the SPS sintering process, one should notice that the grain boundary contribution is not observed for a temperature higher than 320 °C, likely due to the overlapping of intra-granular and inter-granular impedances. Over the

entire working temperature range, the calculated activation energy ($E_A \approx 1.0$ eV) and ionic conductivity of the solid electrolyte are also in good agreement with the previously reported values. Concerning the single phase cells Au/$NaNb_{1-x}Ti_xO_{3-0.5x}$/Au (x = 0, 0.10), the results are reported on **Figure 5**a-c as well. For both compounds, only one depressed semi-circle is observed in the HF and MF range. Additionally, the associated capacitive effect ($C_{eq} \approx 5\times10^{-10}$ F) remains within the same order of magnitude versus the temperature, meaning that no significant change occurs in the ceramic sample. This impedance contribution is used to calculate the total conductivity of the sample σ_{total}. Finally, for both sandwich–type cells YSZ-8/$NaNb_{1-x}Ti_xO_{3-0.5x}$/YSZ-8 (x = 0, 0.10), the HF relaxation frequencies and equivalent capacitive effects (f_{relax} and C_{eq}) are similar to the YSZ-8 bulk impedance in the studied working temperature range. Consequently, no Na^+ diffusion occurs into the YSZ-8 materials, in agreement with SEM on the native fully oxidized sandwich-type samples. According to this electrochemical behavior, the HF impedance contribution can be assigned to the pure O^{2-} ionic conductivity in the YSZ-8 layer. Concerning the MF impedance observed in the sandwich-type samples, this additional contribution is assigned to the the pure O^{2-} ionic conductivity through the niobate compounds. For the sandwiched pellets including $NaNb_{1-x}Ti_xO_{3-0.5x}$ (x = 0, 0.10) oxides, the higher the ionic conduction of the material, the higher the relaxation frequency (**Figure 5c**), meaning that the ionic transfer at the interface $NaNb_{1-x}Ti_xO_{3-0.5x}$/YSZ-8 is enhanced. For the sample YSZ-8/$NaNb_{0.9}Ti_{0.1}O_{2.95}$/YSZ-8 in the temperature range RT < T < 400 °C, the different impedance HF and MF contributions can be separated whereas above T = 400 °C, MF impedance contribution from the niobate and HF contribution from YSZ-8 significantly overlap (**Figure S6**). This experimental observation does not allow extracting the O^{2-} ionic conductivity of $NaNb_{0.9}Ti_{0.1}O_{2.95}$ above T = 400°C (**Figure 5c**, dashed red line).

By comparing the MF conductivity ($\sigma_{O2-(MF)}$, green and red triangles in **Figure 5c**) assigned to O^{2-} mobile species in the two niobates, it can be concluded that the titanium-doped sodium

niobate is ca. 100 times more O^{2-} conductive than the undoped $NaNbO_3$. These measurements are therefore in good agreement with the presence of oxygen vacancies in the framework induced by the Ti^{4+} substitution on Nb^{5+} sites. For both samples considered seperately, the contribution of sodium and oxygen to total ionic conductivity is evaluated in the next section through the calculation of ionic transport numbers.

2.4. Ionic transport numbers

On the basis of the EIS measurements performed on single-phase pellets $NaNbO_3$ and $NaNb_{0.9}Ti_{0.1}O_{2.95}$ compared to the Na^+ symmetrical blocking layer (sandwich-type cells), the oxygen and sodium ionic transport numbers are deduced according to **Equation 6** and **7**, respectively:

$$t_{O^{2-}} = \frac{\sigma_{O^{2-}}}{\sigma_{Na^+}+\sigma_{O^{2-}}+\sigma_{e^-}} = \frac{\sigma_{O^{2-}}}{\sigma_{total}} \quad (6)$$

$$t_{Na^+} = \frac{\sigma_{Na^+}}{\sigma_{Na^+}+\sigma_{O^{2-}}+\sigma_{e^-}} = \frac{\sigma_{Na^+}}{\sigma_{total}} \quad (7).$$

The sodium ionic conductivity (σ_{Na+}) is thus obtained from the subtraction of the contribution of oxygen $\sigma_{O2-(MF)}$ (measured with blocking layers) to the total conductivity σ_{total} (measured without blocking layers).

Based on the EIS measurements involving the sandwiched pellet Au/YSZ-8/$NaNb_{1-x}Ti_xO_{3-0.5x}$/YSZ-8/Au and only titanium-doped sodium niobates Au/$NaNb_{1-x}Ti_xO_{3-0.5x}$/Au, the sodium and oxygen ionic transport numbers can be estimated separately. In pure sodium niobate (x = 0), Na^+ ions are the majority mobile species with $t_{Na+} \approx 88\%$, independent of temperature (**Figure 6**). However, the substitution of Ti^{4+} for Nb^{5+} up to 10 % leads to the creation of oxygen vacancies, inducing oxygen mobility. Starting with the pristine material ($NaNbO_3$) where Na^+ conductivity is dominant, the O^{2-} mobility should also take place in the Ti-substituted complex oxide. From around 220 °C to 350 °C, the contribution of O^{2-} progressively increases over Na^+. For higher temperatures, several contributions overlap on the impedance spectrum for the

sandwiched pellet. The overlap leads to higher uncertainty on the conductivity. When the conductivity for the sandwiched pellet is higher than that of the single $NaNb_{0.9}Ti_{0.1}O_{2.95}$, which has no physical meaning, the transport number of O^{2-} is considered close to unity $t_{O2-} = 1$ (dashed red line).. In this high temperature range, the Na^+ ionic conductivity is then neglected. Comparing $NaNbO_3$ and $NaNb_{0.9}Ti_{0.1}O_{2.95}$ above T = 350 °C, the increase of total conductivity when substituting Ti^{4+} for Nb^{5+} is thus experimentally demonstrated to originate from the introduction of oxygen vacancies for the first time, confirming assumptions made by comparing activation energies that are hardly valuable when it comes to potential mixed ionic conduction.

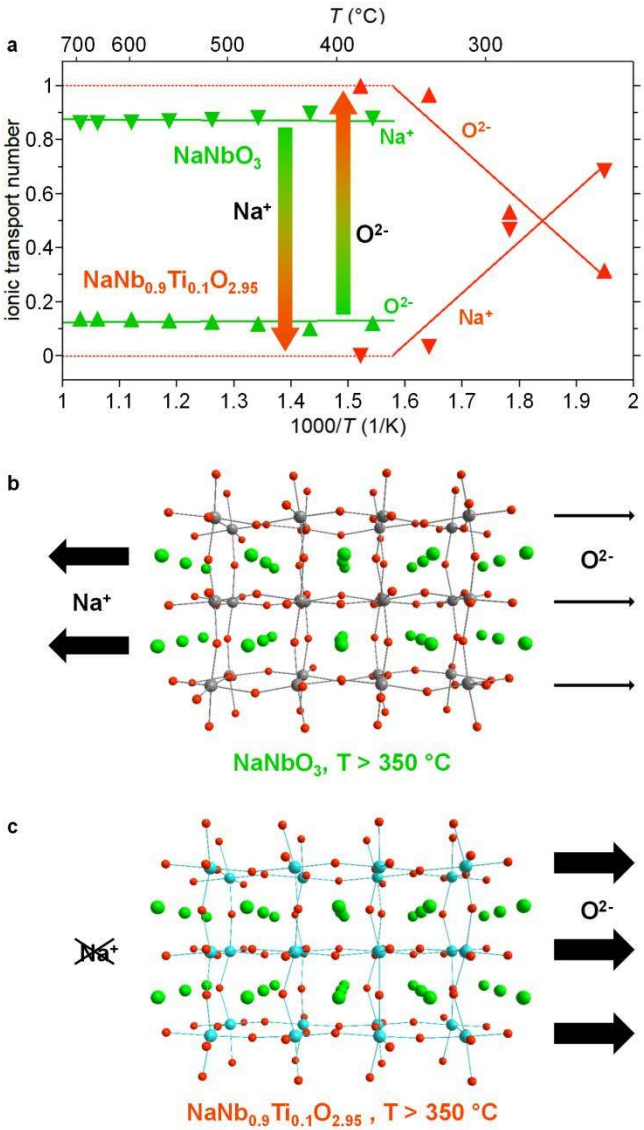

Figure 6. a) Inversion in Na^+ and O^{2-} transport numbers between b) $NaNbO_3$ (Na^+ major, O^{2-} minor) and c) $NaNb_{0.9}Ti_{0.1}O_{2.95}$ (O^{2-} exclusive) above 350 °C.

3. Discussion

In summary, the blocking electrolyte method characterized by electrochemical impedance spectroscopy measurements allows one to separately estimate the contributions of two mobile ionic species in a perovskite framework. The evaluation of the transport ionic numbers of Na^+ and O^{2-} carriers in the same network has never been undertaken before, and this knowledge will enable designing new frameworks with tuned mixed ionic conductivities.

SPS proved to be a valuable technique to design dense pellets with complex sandwich-type architecture.[58] In the case of Nb- and Ti-based materials, the sintering is associated primarily with vacuum (ca. 10 Pa), high temperatures (900 to 1200 °C), a strong electric current (several Amperes) and an elemental carbon-based environment. These combined conditions are responsible for the formation of paramagnetic Nb^{4+} and Ti^{3+} together with oxygen vacancies, leading to a semiconducting behavior with electronic conductivity ($\sigma = 10^{-4}$ S.cm^{-1} at T = 200 °C and low activation energy of 0.14 eV for $NaNbO_{3-x}$). During a conventional heat treatment, full reoxidation occurs at 550-600 °C, even under inert gas ($P_{O2} = 2\times10^{-5}$ atm), thus revealing a pure ionic conductivity for the sodium niobate. Interestingly, major reorganization of Na and O atomic positions occurs around 550 °C, with a structural transition from the orthorhombic Cmcm to tetragonal P4/mbm space group. It is proposed that both phenomena are strongly related, although a dedicated study on this temperature range with more resolved data should be performed to definitively draw their interplay.

Symmetrical sodium-blocking/oxygen-specific electrolytes on each side of the sandwich sample enabled measurementof the ionic transport number of O^{2-}, where Na^+ contribution was then obtained by deduction. Reciprocally, using NASICON or β-Alumina as O^{2-} blocking layers would allow the estimation of the t_{Na+} sodium ionic transport numbers and to deduce the t_{O2-} oxygen ionic transport number. In the pure sodium niobate, both Na^+ (t_{Na+} = 88 %) and O^{2-} (t_{O2-} = 12 %, independent of temperature) contributeto the conductivity in a poor ion conductor.

Accordingly, vacancy formation does not occur in either the Na site or in the O site after the annealing treatment under air. The activation energy of 0.83 eV related to $NaNbO_3$ is close to values found in perovskite-derived frameworks such as $Na_{3x}La_{1.33-x}\square_{0.67-2x}Ti_2O_6$ (0.92 eV)[39] rather than in Na/Zr/Mg-based silicate-phosphates (0.25 eV).[22] The slightly smaller value compared to the titanate can be attributed to facilitated Na diffusion pathways, limited by smaller bottlenecks formed by four adjacent [TiO_6] octahedra in $Na_{3x}La_{1.33-x}\square_{0.67-2x}Ti_2O_6$ (average Ti-O distance of 1.95 Å)[39] than four adjacent [NbO_6] in $NaNbO_3$ (Nb-O distances from 1.90 to 2.09 Å, average 1.97 Å).[56] For both oxygen and sodium, the absence of site vacancy accounts for poor overall conductivity. However, the O^{2-} mobility is sufficient to compete with Na^+ carrier displacements which are mainly governed by steric effects (e.g. bond distances) coordination number and diffusion paths with energy barriers. More interestingly, the thermal activation of the conductivity is quantitatively the same when either both carriers or only oxygen are enabled, suggesting a correlation to be elucidated between the two carriers. Ionic transport numbers depend more strongly on temperature in $NaNb_{0.9}Ti_{0.1}O_{2.95}$ complex oxide. O^{2-} progressively takes over Na^+ up to around T = 350 °C. Above T = 350 °C, the O^{2-} contribution switches from minor in $NaNbO_3$ to exclusive in $NaNb_{0.9}Ti_{0.1}O_{2.95}$ complex oxide, given some uncertainty on the conductivity measurement of the sandwich-type pellet. Both the introduction of O vacancies and a positive effect from competitive bonds affect Na1(2)-O1(2)-Nb-O3(4), stabilizing the $P2_1ma$ structure which leads to dramatic enhancement of the overall conductivity, and a significant decrease of the activation energy. The strong variation of Na1-O1 and Na2-O2 bond lengths after Ti substitution leads to the reduction of the Nb/Ti-O1 and Nb/Ti-O2 apical distortions (elongation of the Nb(Ti)O_6 octahedra compared to NbO_6 polyhedra in Pbma-$NaNbO_3$), and consequently to distortion in the equatorial plane.[57] Therefore, Ti^{4+} substitution for Nb^{5+} ions and the creation of oxygen vacancies in the perovskite network lead to an increased transition of metal crystal-field splitting, as well as the SOJT effect and Nb(Ti)-O bond covalency.

In the case of $NaNb_{0.9}Ti_{0.1}O_{2.95}$, the ionic conductivity varies between 1.8×10^{-5} and 6×10^{-4} $S.cm^{-1}$ in the interval 350-530 °C. This material cannot be referred as a Na^+/O^{2-} mixed conductor in this temperature range. While both ionic species take part in the overall ion conductivity in $NaNbO_3$ with a 88/12 transport number ratio, an ideal electrochemical cell using a Na^+/O^{2-} mixed ionic conductor as solid electrolyte has an optimized transport number ratio of 50/50. Such a ratio could be found in $NaNb_{1-x}Ti_xO_{3-0.5x}$ for a single x value comprised between 0 and 0.10. However, Ti-substituted sodium niobates can stabilize higher O-deficiency concentrations, at the origin of even higher oxygen ionic conductivity.[28,57] Strategies to improve Na^+ contributions in a high Na^+/O^{2-} mixed ion conductor are discussed hereafter.

First, it is noteworthy that in NASICON or β-alumina as well as in LISICON or Li-garnet, the strong covalence of phosphate(silicate) groups in NASICON and LISICON, Al^{3+}-based spinel blocks in β-alumina, and Zr-O bonds in Li-garnet prevent any creation of oxygen vacancies in these oxide frameworks. Therefore, ion conduction involving both Na^+ and O^{2-} species with comparable mobilities in the same temperature range necessarly occurs best in oxygen-conductor frameworks. Sodium niobate has been chosen because it crystallizes with a derived-perovskite lattice. This is a structure well investigated for oxygen mobility, as oxygen vacancies can be induced by substitution of low valent cations. Furthermore, Nb^{5+} ions adopt a second order Jahn-Teller (SOJT) distortion and the octahedra remain highly distorted in the equatorial planes (Pbma space group), alternating shorter (1.90 Å) to longer (2.09 Å) bond lengths with various octahedral tilting in three different directions. Such a SOJT distortion emphasizes the enhanced oxygen mobility.

From solid-state chemistry, to achieve high oxide ion conduction, oxygen vacancies are created through the partial substitution of a low valent cation for the 6-coordinated octahedral site (B) of the perovskite network; a strategy that can be generalized to other structures. In the perovskite-related structure, ion conduction can also be driven by polarizable cations with 12-fold coordinated to oxygen in the (A) site. This is especially true when the A site is partially

vacant, again due to the stabilization of the low valent cation in the B site or the high valent cation in A site (such as Ca^{2+}). The $Ca_2Nb_2O_7$ pyrochlore phase can be easily stabilized.[71,72] From a theoreticalperspective, the stability of the perovskite type is governed by the ionic radii and the well-known Goldschmidt tolerance factor.[73] Taking into account the ionic radius ratio between cations in A and B sites, for $r(A^{n+})/r(B^{m+}) > 1.80$, the 3D- or 2D-perovskite network is generally stabilized, whereas the pyrochlore structure ($A_2B_2O_7$) is obtained for $1.46 < r(A^{n+})/r(B^{m+}) < 1.80$, and finally the fluorite framework is favored for $r(A^{n+})/r(B^{m+}) < 1.46$. The introduction of vacancies on the A site contributes to the creation of cations ordering and forming superstructures, identified, for instance, in hexagonal tungsten bronze (Na_xWO_3).[74,75] Supercells are required to give a pertinent crystallographic description of the structure and cationic conduction properties strongly depend on the pathways available for the cations into the framework. The perovskite, the pyrochlore, and the fluorite-type structures (AO_2) are also among the networks which exhibit the best oxygen mobility associated with the easy formation of oxygen vacancies. In summary, the precise control of structural features in the large perovskite family coupled with controlled introduction of mixed valence in both the A and B sites should lead to high and balanced mixed ionic conductivities. Finally, in order to achieve both sodium and oxygen vacancies in $NaNbO_3$, without aliovalent doping in A and B sites, a possibility is the reaction by SPS between $NaNbO_3$ and either Nb_2O_5 or Nb_2O_5-WO_3 solid-solution.[76–79] In these complex systems, homoepitaxy or epitaxial growth should occur, generating intergrowth at the interface and diffusion to stabilize the defects containing Na^+/O^{2-} vacancies. Such intergrown structures must also be explored among the so-called (i) Ruddlesden-Popper phases with alternating perovskite blocks and rocksalt-type layers, and (ii) Aurivillius phases which have alternating perovskite blocks with fluorite-like $(Bi_2O_2)^{2+}$ units.[80–84] In these frameworks, Na^+ ionic mobility should take place in a specific unit whereas O^{2-} ionic carriers should migrate into the perovskite blocks, creating independent channels for

mobile species. In these families, interfacial reorganization should be of utmost importance to enhance mixed Na^+/O^{2-} ionic conductivity.

3. Conclusion

Our study provides a simple strategy to independently measure Na^+ and O^{2-} ionic conductivity in a complex oxide, and consequently, to design higher performing mixed ionic conductors. This is exemplified with $NaNbO_3$ and $NaNb_{0.9}Ti_{0.1}O2.95$ in the 350-700 °C temperature range, with major Na^+/minor O^{2-} and exclusive O^{2-} conduction, respectively. The library of derived-perovskite oxides should be revisited, taking this new and promising angle into account. Finally, the concept of Na^+/O^{2-} mixed conductivity should be regarded more generally to any anion/cation couple; for instance, considering Li^+ instead of Na^+.

4. Experimental Section

Synthesis: 0.810 g Nb_2O_5 (99.9 %, Sigma-Aldrich) was suspended in 20 mL of NaOH (6 M) and heated in an autoclave equipped with 40 mL Teflon vials, using a P330 oven (Nabertherm). The sample was heated to 200 °C for 24 h, with heating and cooling ramp rates of 2°C min^{-1}. The white sediment and supernatant were both transferred in a 200 mL centrifuge tube (Nalgene) and centrifuged (Sigma 3-30K apparatus) 15 min at 7 krpm. The supernatant was removed, the pellet was dispersed in approx. 100 mL of deionized water, and the dispersion was centrifuged 15 min at 7 krpm. The separation, dispersion, and centrifugation process was repeated once. Finally, the supernatant was removed and the pellet was dried at 80 °C overnight. Annealing treatments were performed under air in tubular ovens connected to a Eurotherm temperature controller. $NaNbO_3$ structures of Pbma and $P2_1ma$ space groups were obtained after 24 h at 950 °C and 6 h at 600 °C, respectively, with systematic 2 °C min^{-1} heating and cooling ramp rates.

Spark Plasma Sintering: For the $NaNbO_3$ and ZrO_2-TZY sample, 0.8 g of powder from hydrothermal synthesis and 0.9 g of ZrO_2 doped with Y_2O_3 (8 $\%_{mol.}$) (Tosoh 8Y, > 99.5 %), respectively, was introduced in a 10 mm graphite dye covered with Papyex. For the sandwiched sample, (i) ZrO_2-TZY (0.45 g), (ii) $NaNbO_3$ from hydrothermal synthesis (0.55 g) and (iii) ZrO_2-TZY (0.45 g) again were consecutively introduced in a 10 mm graphite dye, with intermediate manual compaction, taking special care of the planarity of the surface before adding another powder. SPS experiments were performed on a 515S Syntex (Dr. Sinter) apparatus. A dynamic vacuum at approx. 10 Pa was maintained during the experiments. For $NaNbO_3$, the temperature was monitored using a thermocouple. The uniaxial pressure was increased to 7.9 kN (100 MPa) in 1 min prior to heating the sample at 50 °C min^{-1} to 900 °C and maintaining it at 900 °C during 5 min. The sample was left to cool 1 min and then the pressure was released from 7.9 to 0.5 kN (minimal charge) in 3 min. For ZrO_2-TZY and ZrO_2-TZY/$NaNbO_3$/ZrO_2-TZY, the temperature of the sample was followed using a pyrometer (sensitivity starting at approx. 600 °C). The sample was heated to 600 °C in 4 min and then at 600 °C for 3 min. In the meantime, uniaxial pressure of 7.9 kN (100 MPa) was applied in 1 min at the beginning of the heating and maintained constant. The sample was heated from 600 to 1000 °C at 100 °C min^{-1} and then 1000 to 1100 °C at 50 °C min^{-1}. After heating 10 min at 1100 °C, the temperature was decreased linearly to 600 °C in 20 min. The pressure was released 1 min after the sample cooled down to 600 °C, from 7.9 to 0.5 kN in 3 min. All samples were polished using abrasive SiC sandpaper with increasing grit sizes from 120 to 2400.

Powder X-ray diffraction: XRD was performed on a PANalytical X'pert PRO MPD apparatus equipped with an X'Celerator multichannel detector. $CuK_{\alpha 1}/K_{\alpha 2}$ radiations were generated at 45 kV and 40 mA. Data were acquired on the reflexion Bragg-Brentano θ-θ mode, $8° \leq 2\theta \leq 80°$ with 0.017 ° steps, acquisition time of 6 h 37 min. Samples were prepared from softened powder (particle size < 45 µm) flattened with the edge of a razor blade to avoid any

preferential orientation. Refinements were performed on JANA2006 software.[85] Isotropic displacement parameters β_{iso} were always maintained at 0.5 for Nb and 1 for Na and O.

^{93}Nb nuclear magnetic resonance: NMR spectra were acquired at a 11.7 T static magnetic field (Larmor frequency: 122.3 MHz) with a single pulse excitation of 1.5 µs (RF field strength: *ca.* 166 kHz) and a recycling delay of 0.2 s. Magic angle spinning (MAS) experiments were performed at a spinning frequency of 30 kHz with a 2.5 mm Bruker probe. Chemical shifts were calibrated according to a saturated solution of $NbCl_5/CH_3CN$ (δ = 0.0 ppm).

Electron spin resonance: experiments were conducted with a Bruker EMX spectrometer operating at X-Band (9.45 GHz). The presented powder spectra were recorded at room temperature (293 K) with a microwave power of 10 mW and a magnetic field modulation amplitude of 1 mT (frequency: 100 kHz). The magnetic field scale was calibrated using a DPPH standard sample (g=2.0036) and the Bruker software suite (WinEPR and WinSimfonia) was used to analyze the observed ESR signals.

Diffuse reflectance: spectra were recorded on powders in the 200-800 nm range from measurements obtained on a Carry-Varian 5000, in integrating sphere configuration. MgO powder was used as a white reference.

Scanning electron microscopy – energy-dispersive X-ray spectrometry: Data were obtained on a JSM 6700F (JEOL) field emission gun SEM equipped with an EDX detector. Acceleration tension of the source was 5 kV for low-magnification imaging and 20 kV for medium- and high-magnification imaging as well as EDX mapping. The sample was fixed to a conductive carbon scotch and an approx. 10 nm-thick Au-Pd layer was deposited to ensure conductivity.

Complex impedance spectroscopy: densified pellets from SPS were analyzed. A thin film of metallic gold electrodes was deposited on both sides of the pellets by sputtering in partial argon atmosphere for 15 min to achieve a homogenous compact gold film. A two-electrode configuration was used for complex impedance spectroscopy measurements. An Autolab

Frequency Response Analyser, applied a signal with a 200 mV amplitude in the 100 mHz-1 MHz frequency range, with 10 steps per decade. Nyquist diagrams were recorded from 200°C to 900°C under argon atmosphere. Equilibrium time (at least 1 hour) has been respected before each measurement during the heating and cooling thermal cycle in order to achieve ready state conditions. The data were analyzed using ZView 2 software of Scribner Associate Inc.

Supporting Information
Supporting Information is available from the Wiley Online Library or from the author.

Acknowledgements
This work was supported by Solvay and CNRS. The authors thank Austin W. Keller for editing the manuscript.

Received: ((will be filled in by the editorial staff))
Revised: ((will be filled in by the editorial staff))
Published online: ((will be filled in by the editorial staff))

[1] D. H. Whitmore, *J. Cryst. Growth* **1977**, *39*, 160.

[2] S. P. S. Badwal, K. Foger, *Ceram. Int.* **1996**, *22*, 257.

[3] Y. Aoki, C. Wiemann, V. Feyer, H. S. Kim, C. M. Schneider, H. Ill-Yoo, M. Martin, *Nat. Commun.* **2014**, *5*, 3473.

[4] N. Mahato, A. Banerjee, A. Gupta, S. Omar, K. Balani, *Prog. Mater. Sci.* **2015**, *72*, 141.

[5] J. Kim, A. Jun, O. Gwon, S. Yoo, M. Liu, J. Shin, T. H. Lim, G. Kim, *Nano Energy* **2018**, *44*, 121.

[6] S. B. Adler, *Chem. Rev.* **2004**, *104*, 4791.

[7] P. M. Geffroy, A. Pons, E. Béchade, O. Masson, J. Fouletier, *J. Power Sources* **2017**, *360*, 70.

[8] M. Sathiya, G. Rousse, K. Ramesha, C. P. Laisa, H. Vezin, M. T. Sougrati, M. L.

Doublet, D. Foix, D. Gonbeau, W. Walker, A. S. Prakash, M. Ben Hassine, L. Dupont, J. M. Tarascon, *Nat. Mater.* **2013**, *12*, 827.

[9] A. Grimaud, W. T. Hong, Y. Shao-Horn, J.-M. Tarascon, *Nat. Mater.* **2016**, *15*, 121.

[10] G. Assat, D. Foix, C. Delacourt, A. Iadecola, R. Dedryvère, J. M. Tarascon, *Nat. Commun.* **2017**, *8*, 2219.

[11] H. Aono, E. Sugimoto, Y. Sadaoka, N. Imanaka, G. Adachi, *Solid State Ionics* **1990**, *40–41*, 38.

[12] R. Murugan, V. Thangadurai, W. Weppner, *Angew. Chemie Int. Ed.* **2007**, *46*, 7778.

[13] K. Fu, Y. Gong, S. Xu, Y. Zhu, Y. Li, J. Dai, C. Wang, B. Liu, G. Pastel, H. Xie, Y. Yao, Y. Mo, E. Wachsman, L. Hu, *Chem. Mater.* **2017**, *29*, 8037.

[14] M. D. Slater, D. Kim, E. Lee, C. S. Johnson, *Adv. Funct. Mater.* **2013**, *23*, 947.

[15] N. Yabuuchi, K. Kubota, M. Dahbi, S. Komaba, *Chem. Rev.* **2014**, *114*, 11636.

[16] K. Vignarooban, R. Kushagra, A. Elango, P. Badami, B. E. Mellander, X. Xu, T. G. Tucker, C. Nam, A. M. Kannan, *Int. J. Hydrogen Energy* **2016**, *41*, 2829.

[17] J.-Y. Hwang, S.-T. Myung, Y.-K. Sun, *Chem. Soc. Rev.* **2017**, *46*, 3529.

[18] H. Y.-P. Hong, *Mater. Res. Bull.* **1976**, *11*, 173.

[19] J. B. Goodenough, H. Y.-P. Hong, J. A. Kafalas, *Mater. Reserch Bull.* **1976**, *11*, 203.

[20] S. Xin, Y.-X. Yin, Y.-G. Guo, L.-J. Wan, *Adv. Mater.* **2014**, *26*, 1261.

[21] S. Wei, S. Xu, A. Agrawral, S. Choudhury, Y. Lu, Z. Tu, L. Ma, L. A. Archer, *Nat. Commun.* **2016**, *7*, 11722.

[22] S. Song, H. M. Duong, A. M. Korsunsky, N. Hu, L. Lu, *Sci. Rep.* **2016**, *6*, 32330.

[23] K. B. Hueso, M. Armand, T. Rojo, *Energy Environ. Sci.* **2013**, *6*, 734.

[24] J. B. Goodenough, *Acc. Chem. Res.* **2013**, *46*, 1053.

[25] S. M. Whittingham, R. A. Huggins, *J. Chem. Phys.* **1971**, *54*, 414.

[26] A. Imai, M. Hirata, *Jpn. J. Appl. Phys.* **1972**, *11*, 180.

[27] B. Dunn, H. Kamath, J. Tarascon, *Science.* **2011**, *334*, 928.

[28] H. Xu, Y. Su, M. Lou Balmer, A. Navrotsky, *Chem. Mater.* **2003**, *15*, 1872.

[29] Y. Li, R. Gemmen, X. Liu, *J. Power Sources* **2010**, *195*, 3345.

[30] Y. Wang, W. D. Richards, S. P. Ong, L. J. Miara, J. C. Kim, Y. Mo, G. Ceder, *Nat. Mater.* **2015**, *14*, 1026.

[31] X. He, Y. Zhu, Y. Mo, *Nat. Commun.* **2017**, *8*, 15893.

[32] V. V Kharton, F. M. B. Marques, A. Atkinson, *Solid State Ionics* **2004**, *174*, 135.

[33] A. Watanabe, *Solid State Ionics* **1995**, *79*, 84.

[34] B. C. H. Steele, A. Heinzel, *Nature* **2001**, *414*, 345.

[35] V. Thangadurai, G. N. Subbanna, A. K. Shukla, J. Gopalakrishnan, *Chem. Mater.* **1996**, *8*, 1302.

[36] M. Li, M. J. Pietrowski, R. A. De Souza, H. Zhang, I. M. Reaney, S. N. Cook, J. A. Kilner, D. C. Sinclair, *Nat. Mater.* **2014**, *13*, 31.

[37] R. A. De Souza, *Adv. Funct. Mater.* **2015**, *25*, 6326.

[38] S. Fop, E. J. Wildman, J. T. S. Irvine, P. A. Connor, J. M. S. Skakle, C. Ritter, A. C. McLaughlin, *Chem. Mater.* **2017**, *29*, 4146.

[39] A. I. Ruiz, M. L. López, C. Pico, M. L. Veiga, *J. Solid State Chem.* **2002**, *163*, 472.

[40] Y. Saito, H. Takao, T. Tani, T. Nonoyama, K. Takatori, T. Homma, T. Nagaya, M. Nakamu, *Nature* **2004**, *432*, 84.

[41] E. Cross, *Nature* **2004**, *432*, 24.

[42] E. Ringgaard, T. Wurlitzer, *J. Eur. Ceram. Soc.* **2005**, *25*, 2701.

[43] J. Rödel, K. G. Webber, R. Dittmer, W. Jo, M. Kimura, D. Damjanovic, *J. Eur. Ceram. Soc.* **2015**, *35*, 1659.

[44] V. A. Shuvaeva, M. Y. Antipin, R. S. V. Lindeman, O. E. Fesenko, V. G. Smotrakov, Y. T. Struchkov, *Ferroelectrics* **1993**, *141*, 307.

[45] M. D. Peel, S. E. Ashbrook, P. Lightfoot, *Inorg. Chem.* **2013**, *52*, 8872.

[46] B. Cai, J. Schwarzkopf, E. Hollmann, D. Braun, M. Schmidbauer, T. Grellmann, R.

Wördenweber, *Phys. Rev. B* **2016**, *93*, 224107.

[47] L. Chao, Y. Hou, M. Zheng, Y. Yue, M. Zhu, *Appl. Phys. Lett.* **2017**, *110*, 122901.

[48] A. M. Glazer, H. D. Megaw, *Acta Crystallogr. Sect. A* **1973**, *29*, 489.

[49] M. Ahtee, A. M. Glazer, *Acta Crystallogr. Sect. A* **1976**, *32*, 434.

[50] A. D. Handoko, G. K. L. Goh, *Green Chem.* **2010**, *12*, 680.

[51] S. K. Mishra, R. Mittal, V. Y. Pomjakushin, S. L. Chaplot, *Phys. Rev. B* **2011**, *83*, 134105.

[52] M. D. Peel, S. P. Thompson, A. Daoud-Aladine, S. E. Ashbrook, P. Lightfoot, *Inorg. Chem.* **2012**, *51*, 6876.

[53] V. S. Bondarev, A. V Kartashev, M. V Gorev, I. N. Flerov, E. I. Pogorel'tsev, M. S. Molokeev, S. I. Raevskaya, D. V Suzdalev, I. P. Raevskii, *Phys. Solid State* **2013**, *55*, 821.

[54] A. C. Sakowski-Cowley, K. Łukaszewicz, H. D. Megaw, *Acta Crystallogr. Sect. B* **1969**, *25*, 851.

[55] K. E. Johnston, C. C. Tang, J. E. Parker, K. S. Knight, P. Lightfoot, S. E. Ashbrook, *J. Am. Chem. Soc.* **2010**, *132*, 8732.

[56] G. Gouget, M. Duttine, E. Durand, A. Villesuzanne, V. Rodriguez, F. Adamietz, T. Le Mercier, M.-D. Braida, A. Demourgues, *ACS Appl. Electron. Mater.* **2019**, *1*, 513.

[57] G. Gouget, M. Duttine, U.-C. Chung, S. Fourcade, F. Mauvy, M.-D. Braida, T. Le Mercier, A. Demourgues, *Chem. Mater.* **2019**, *31*, 2828.

[58] A. Aboulaich, R. Bouchet, G. Delaizir, V. Seznec, L. Tortet, M. Morcrette, P. Rozier, J. M. Tarascon, V. Viallet, M. Dollé, *Adv. Energy Mater.* **2011**, *1*, 179.

[59] M. Chemla, *Ann. Phys. (Paris).* **1956**, *13*, 959.

[60] C. Wagner, *Zeitschrift für Phys. Chemie* **1933**, *21B*, 25.

[61] F. Mauvy, C. Lalanne, J.-M. Bassat, J.-C. Grenier, A. Brisse, A.-L. Sauvet, C. Barthet, J. Fouletier, *Solid State Ionics* **2009**, *180*, 1183.

[62] F. Mauvy, J.-M. Bassat, E. Boehm, P. Dordor, J.-P. Loup, *Solid State Ionics* **2003**, *158*, 395.

[63] F. Mauvy, E. Boehm, J.-M. Bassat, J.-C. Grenier, J. Fouletier, *Solid State Ionics* **2007**, *178*, 1200.

[64] J. Xu, Y. Li, J. Wang, H. Bao, J. Wang, C. Zhu, L. Ye, K. Xie, X. Kuang, *Adv. Electron. Mater.* **2018**, *4*, 1800352.

[65] E. Boehm, J.-M. Bassat, M. C. Steil, P. Dordor, F. Mauvy, J.-C. Grenier, *Solid State Sci.* **2003**, *5*, 973.

[66] A. Mitterdorfer, L. J. Gauckler, *Solid State Ionics* **1998**, *111*, 185.

[67] K. V. Govindan Kutty, C. K. Mathews, T. N. Rao, U. V. Varadaraju, *Solid State Ionics* **1995**, *80*, 99.

[68] E. J. L. Schouler, N. Mesbahi, G. Vitter, *Solid State Ionics* **1983**, *9–10*, 989.

[69] F. Mauvy, C. Lalanne, J.-M. Bassat, J.-C. Grenier, H. Zhao, L. Huo, P. Stevens, *J. Electrochem. Soc.* **2006**, *153*, A1547.

[70] F. Mauvy, J.-M. Bassat, E. Boehm, J.-P. Manaud, D. P., J.-C. Grenier, *Solid State Ionics* **2003**, *158*, 17.

[71] M. A. Subramanian, G. Aravamudan, G. V Subba Rao, *Prog. Solid State Chem.* **1983**, *15*, 55.

[72] O. G. D'yachenko, S. Y. Istomin, A. M. Abakumov, E. V. Antipov, *Inorg. Mater.* **2000**, *36*, 247.

[73] V. M. Goldschmidt, *Trans. Faraday Soc.* **1929**, 253.

[74] J. F. Smith, G. C. Danielson, *J. Chem. Phys.* **1954**, *22*, 266.

[75] F. Takusagawa, R. A. Jacobson, *J. Solid State Chem.* **1976**, *18*, 163.

[76] S. Andersson, *Acta Chem. Scand.* **1967**, *21*, 1777.

[77] S. Iijima, J. G. Allpress, *Acta Crystallogr. Sect. A* **1974**, *30*, 22.

[78] H. Obayashi, J. S. Anderson, *J. Solid State Chem.* **1976**, *17*, 79.

[79] M. Sundberg, B.-O. Marinder, *J. Solid State Chem.* **1990**, *84*, 23.

[80] K. Toda, Y. Kameo, M. Fujimoto, M. Sato, *J. Ceram. Soc. Japan* **1994**, *102*, 737.

[81] K. Toda, Y. Kameo, S. Kurita, M. Sato, *J. Alloys Compd.* **1996**, *234*, 19.

[82] S. Byeon, K. Park, *J. Solid State Chem.* **1996**, *121*, 430.

[83] R. E. Schaak, T. E. Mallouk, *Chem. Mater.* **2002**, *14*, 1455.

[84] Z. S. Gönen, D. Paluchowski, P. Zavalij, B. W. Eichhorn, J. Gopalakrishnan, *Inorg. Chem.* **2006**, *45*, 8736.

[85] V. Petrícek, M. Dušek, L. Palatinus, *Zeitschrift fur Krist.* **2014**, *229*, 345.

TOC:
The transport numbers of sodium cations and oxygen anions are quantified in niobate pervoskites via an original method using sandwiched pellets with solid Na^+-blocking/O-conducting layers. Above 350 °C, charge carriers switch from major Na^+/minor O^{2-} for $NaNbO_3$ to exclusive O^{2-} for $NaNb_{0.9}Ti_{0.1}O_{2.95}$. This first evidence of mixed-ion Na^+/O^{2-} underlies a novel strategy towards improved ionic conductivity in perovskite-derived structures.

Keyword Charge Transport

*G. Gouget, F. Mauvy, U-C. Chung, S. Fourcade, M. Duttine, M.-D. Braida, T. Le Mercier, A. Demourgues**

Associating and Tuning Sodium and Oxygen Mixed-ion Conduction in Niobium-based Perovskites

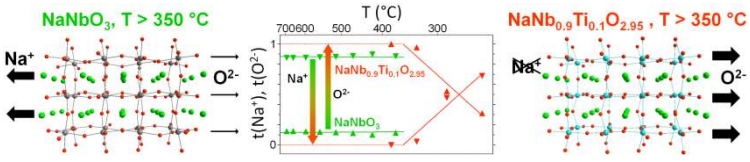

Supporting Information

Associating and Tuning Sodium and Oxygen Mixed-ion Conduction in Niobium-based Perovskites

*Guillaume Gouget, Fabrice Mauvy, U-Chan Chung, Sébastien Fourcade, Mathieu Duttine, Marc-David Braida, Thierry Le Mercier, and Alain Demourgues**

Table S1. Unit cell parameters, atomic coordinates and thermal displacements refined in the Pbma space group by XRD Rietveld analysis of sodium niobate powder annealed under air at T = 950°C and powdered dense ceramic from SPS at T = 900 °C under primary vacuum).

		$NaNbO_3$[a] air, 950 °C	$NaNbO_{3-x}$ SPS, 900 °C
a (Å)		5.5693(1)	5.5675(2)
b (Å)		15.5177(3)	15.5123(4)
c (Å)		5.5046(1)	5.5036(2)
V (Å^3)		475.72(1)	475.32(2)
ε (nm)		174(3)	114(2)
Rp (%)		4.15	4.28
wRp (%)		5.33	5.51
Rall (%)		4.26	4.30
wRall (%)		4.42	4.72
Nb	x	0.26979(19)	0.2660(3)
	y	0.1249(2)	0.1248(4)
	z	0.2423(3)	0.2573(4)
Na1	x	0.75	0.75
	y	0	0
	z	0.2607(16)	0.239(2)
Na2	x	0.7853(11)	0.7911(13)
	y	0.25	0.25
	z	0.2611(17)	0.239(2)
O1	x	0.25	0.25
	y	0	0
	z	0.302(3)	0.314(3)
O2	x	0.249(2)	0.263(3)
	y	0.25	0.25
	z	0.176(2)	0.189(3)
O3	x	0.0343(18)	0.050(2)
	y	0.1460(6)	0.1440(9))
	z	0.5327(13)	0.5385(15)
O4	x	0.4602(14)	0.464(2)
	y	0.1134(7)	0.1135(10)
	z	-0.0417(13)	-0.0325(18)
β_{iso}(Nb) (Å^2)		0.5	0.5
β_{iso}(Na) (Å^2)		1	1
β_{iso}(O) (Å^2)		1	1

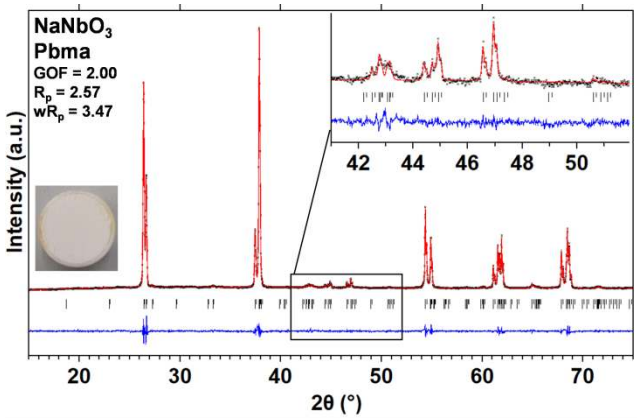

Figure S1. XRD profile matching (Co $K_\alpha 1/K_\alpha 2$ source used here, λ = 1.7890 and 1.7919 Å) of $NaNbO_3$ after SPS at 900 °C followed by annealing under air at 900 °C (dense pellet).

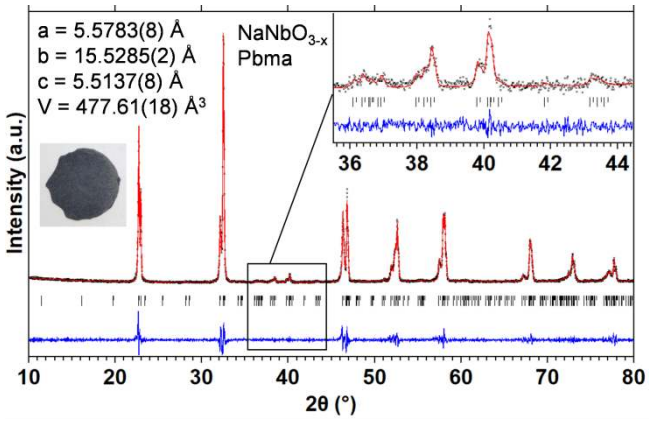

Figure S2. Profile matching of $NaNbO_3$ structure in the Pbma space group after SPS at 1200 °C during 5 min. GOF = 1.54, Rp = 8.59, wRp = 11.26.

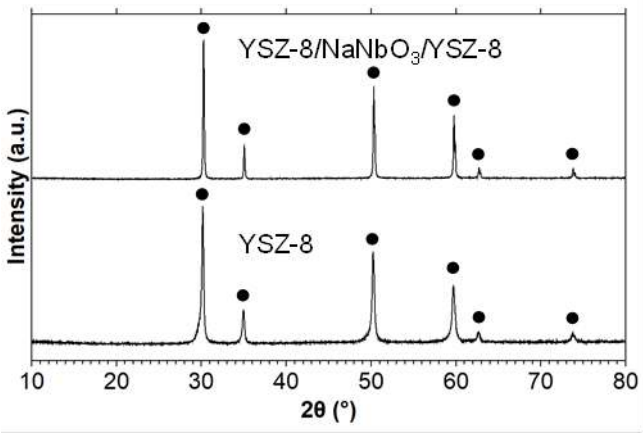

Figure S3. XRD of the YSZ-8 pellet after SPS at 1100 °C during 10 min and the sandwich-type pellet YSZ-8/$NaNbO_3$/YSZ-8 after SPS at 1100 °C during 10 min followed by annealing under air at 800 °C during 12 h. black circles: indexation along yttrium and zirconium oxide 92 ZrO_2.8 Y_2O_3, ICDD 00-030-1468.

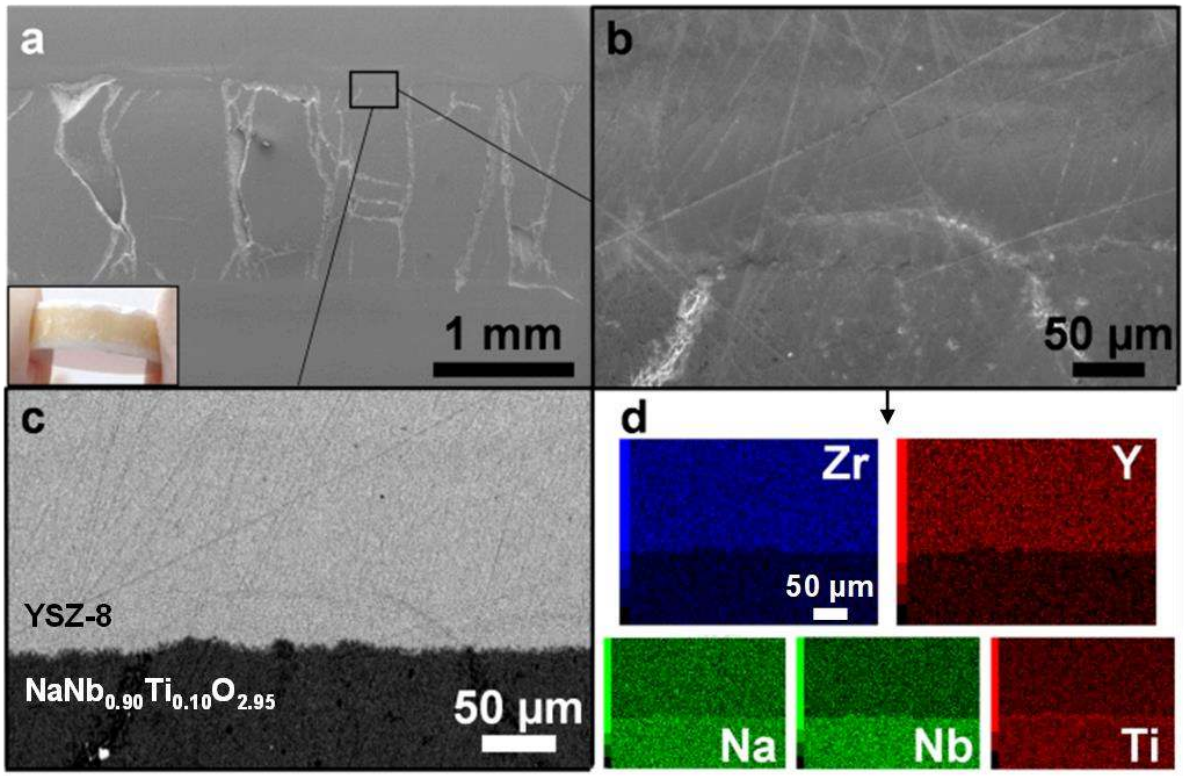

Figure S4. SEM pictures and EDX mapping at the YSZ-8/$NaNb_{0.9}Ti_{0.1}O_{2.95}$ interface. Cross-section view of the sandwiched pellet.

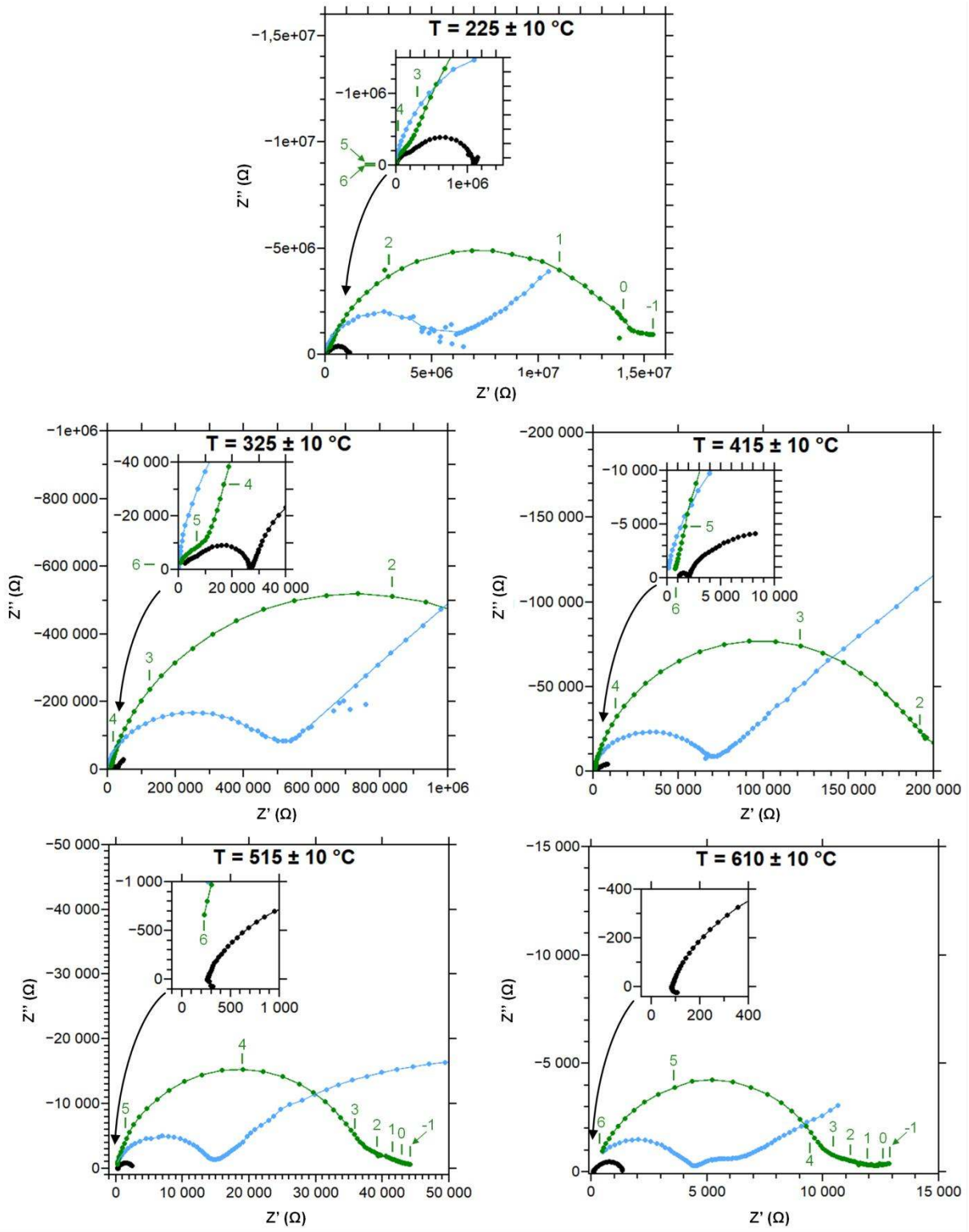

Figure S5. Nyquist diagrams of (black) YSZ-8, (light blue) $NaNbO_3$ and (green) YSZ-8/$NaNbO_3$/YSZ-8 for temperatures comprised between 200 and 600 °C. The numbers reported in the figure are the frequency logarithms.

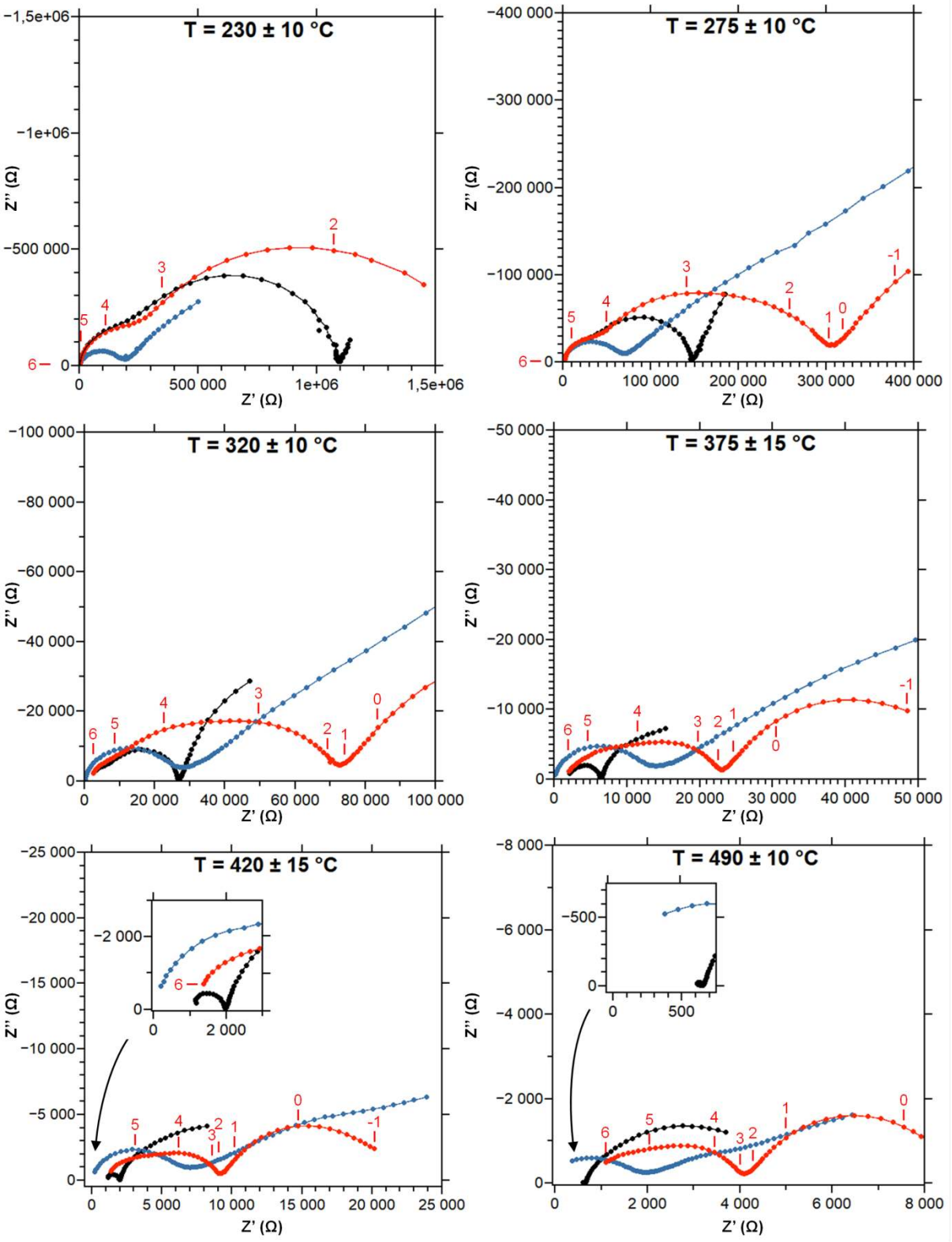

Figure S6. Nyquist diagrams of (black) YSZ-8, (deep blue) $NaNb_{0.9}Ti_{0.1}O_{2.95}$ and (red) YSZ-8/$NaNb_{0.9}Ti_{0.1}O_{2.95}$/YSZ-8 for temperatures comprised between 200 and 500 °C. The numbers reported in the figure are the frequency logarithms.

Table S2. Geometrical dimensions of pellets and fit results of impedance diagrams recorded at approx. 325 °C for YSZ-8, $NaNbO_3$ and YSZ-8/$NaNbO_3$/YSZ-8 samples and 275 °C for YSZ-8, $NaNb_{0.9}Ti_{0.1}O_{2.95}$ and YSZ-8/$NaNb_{0.9}Ti_{0.1}O_{2.95}$/YSZ-8 samples. For sandwich pellets thicknesses, the first value refers to inner niobate layer, the second one to the overall sample.

sample	HF			MF					
	σ (S.cm^{-1})	C (F)	f_{relax} (Hz)	σ_1 (S.cm^{-1})	C_{eq1} (F)	f_{relax1} (Hz)	σ_2 (S.cm^{-1})	C_{eq2} (F)	f_{relax2} (Hz)
YSZ-8 (324 °C)	$4.18\ 10^{-5}$	$8.02\ 10^{-11}$	$3.08\ 10^{5}$	$1.40\ 10^{-5}$	$4.53\ 10^{-10}$	$1.83\ 10^{4}$			
$NaNbO_3$				$8.59\ 10^{-7}$	$3.52\ 10^{-10}$	$1.49\ 10^{3}$			
YSZ-8/$NaNbO_3$/YSZ-8	$2.88\ 10^{-5}$	$9.74\ 10^{-11}$	$1.89\ 10^{5}$	$1.23\ 10^{-7}$	$7.78\ 10^{-10}$	$1.53\ 10^{2}$			
YSZ-8 (278 °C)	$7.12\ 10^{-6}$	$8.71\ 10^{-11}$	$4.83\ 10^{4}$	$2.50\ 10^{-6}$	$4.66\ 10^{-10}$	$3.17\ 10^{3}$			
$NaNb_{0.9}Ti_{0.1}O_{2.95}$				$2.65\ 10^{-6}$	$7.16\ 10^{-10}$	$3.37\ 10^{3}$			
YSZ-8/$NaNb_{0.9}Ti_{0.1}O_{2.95}$/YSZ-8	$8.02\ 10^{-6}$	$8.88\ 10^{-11}$	$5.03\ 10^{4}$	$2.42\ 10^{-6}$	$1.22\ 10^{-9}$	$1.49\ 10^{3}$	$2.96\ 10^{-6}$	$1.08\ 10^{-8}$	$2.05\ 10^{2}$

Table S3. Conductivities (σ_i, i = 1, 2 or 3), equivalent capactities ($C_{eq\,i}$) and relaxation frequencies ($f_{relax\,i}$) for YSZ-8, $NaNbO_3$ and YSZ-8/$NaNbO_3$/YSZ-8. Values are calculated from fitting the Nyquist curves (Figure S5) with R-CPEs in parallel. Conductivities are reported after taking the thickness and surface of the pellets (Table 1) into account. When C_{eq1} and f_{relax1} are not reposrted, σ_1 is considered as Z' for minimal lZ"l.

YSZ-8

		HF			MF			LF		
T (°C)	1000/T (1/K)	σ (S.cm^{-1})	C_{eq} (F)	f_{relax} (Hz)	σ (S.cm^{-1})	C_{eq} (F)	f_{relax} (Hz)	σ (S.cm^{-1})	C_{eq3}(F)	f_{relax3}(Hz)
231	1.98	1.43 10^{-6}	9.15 10^{-11}	9.21 10^{3}	2.92 10^{-7}	3.84 10^{-10}	4.49 10^{2}			
278	1.81	7.12 10^{-6}	8.71 10^{-11}	4.83 10^{4}	2.50 10^{-6}	4.66 10^{-10}	3.17 10^{3}			
324	1.67	4.18 10^{-5}	8.02 10^{-11}	3.08 10^{5}	1.40 10^{-5}	4.53 10^{-10}	1.83 10^{4}	3.13 10^{-6}	3.89 10^{-5}	4.75 10^{-2}
372	1.55	1.44 10^{-4}			6.02 10^{-5}	4.47 10^{-10}	7.95 10^{4}	1.06 10^{-5}	6.10 10^{-5}	1.03 10^{-1}
419	1.44	7.55 10^{-4}			2.61 10^{-4}	6.00 10^{-10}	2.57 10^{5}	2.29 10^{-5}	5.15 10^{-5}	2.62 10^{-1}
476	1.33							7.85 10^{-5}	4.85 10^{-5}	9.56 10^{-1}
526	1.25							1.29 10^{-4}	4.43 10^{-5}	2.12
565	1.19							2.18 10^{-4}	3.74 10^{-5}	3.44
600	1.15							2.40 10^{-4}	3.36 10^{-5}	4.21

$NaNbO_3$

		MF			LF		
T (°C)	1000/T (1/K)	σ (S.cm^{-1})	C_{eq} (F)	f_{relax} (Hz)	σ (S.cm^{-1})	C_{eq} (F)	f_{relax} (Hz)
310	1.71	8.59 10^{-7}	3.52 10^{-10}	1.49 10^{3}	1.69 10^{-6}	4.16 10^{-9}	2.48 10^{2}
409	1.47	5.23 10^{-6}	2.98 10^{-10}	1.07 10^{4}	1.31 10^{-5}	7.10 10^{-9}	1.13 10^{3}
505	1.29	2.74 10^{-5}	2.40 10^{-10}	6.95 10^{4}	5.49 10^{-5}	2.77 10^{-9}	1.21 10^{4}
601	1.14	7.75 10^{-5}	1.88 10^{-10}	2.51 10^{5}	2.24 10^{-4}	7.54 10^{-9}	1.81 10^{4}
702	1.03	2.90 10^{-4}	2.13 10^{-10}	8.31 10^{5}			
799	0.93	5.60 10^{-4}	2.05 10^{-10}	1.67 10^{6}			
894	0.86	1.39 10^{-3}	2.46 10^{-10}	3.45 10^{6}			

YSZ-8/$NaNbO_3$/YSZ-8

		HF			MF		
T (°C)	1000/T (1/K)	σ (S.cm^{-1})	C_{eq} (F)	f_{relax} (Hz)	σ (S.cm^{-1})	C_{eq} (F)	f_{relax} (Hz)
233	1.98	1.40 10^{-6}	1.23 10^{-10}	7.31 10^{3}			
325	1.67	2.88 10^{-5}	9.74 10^{-11}	1.89 10^{5}	1.23 10^{-7}	7.78 10^{-10}	1.53 10^{2}
375	1.54	1.12 10^{-4}	8.93 10^{-11}	8.05 10^{5}	3.78 10^{-7}	6.87 10^{-10}	5.30 10^{2}
425	1.43				8.15 10^{-7}	6.29 10^{-10}	1.25 10^{3}
472	1.34				2.08 10^{-6}	4.90 10^{-10}	4.09 10^{3}
520	1.26				4.39 10^{-6}	4.23 10^{-10}	1.00 10^{4}
570	1.19				8.82 10^{-6}	3.46 10^{-10}	2.46 10^{4}
620	1.12				1.59 10^{-5}	2.41 10^{-10}	6.37 10^{4}
670	1.06				2.71 10^{-5}	2.22 10^{-10}	1.18 10^{5}
698	1.03				3.52 10^{-5}	2.42 10^{-10}	1.40 10^{5}

Table S4. Conductivities (σ_i, i = 1, 2 or 3), equivalent capactities ($C_{eq\,i}$) and relaxation frequencies ($f_{relax\,i}$) for $NaNb_{0.9}Ti_{0.1}O_{2.95}$ and YSZ-8/$NaNb_{0.9}Ti_{0.1}O_{2.95}$/YSZ-8. Values are calculated from fitting the Nyquist curves (Figure S6) with R-CPEs in parallel. Conductivities are reported after taking the thickness and surface of the pellets (Table 1 in main text) into account.

$NaNb_{0.9}Ti_{0.1}O_{2.95}$

		MF			LF			LF		
T (°C)	1000/T (1/K)	σ (S.cm^{-1})	C_{eq} (F)	f_{relax} (Hz)	σ_1 (S.cm^{-1})	C_{eq1} (F)	f_{relax1} (Hz)	σ_2 (S.cm^{-1})	C_{eq2} (F)	f_{relax2} (Hz)
223	2.02	$9.37\,10^{-7}$	$7.91\,10^{-10}$	$1.08\,10^{3}$						
266	1.85	$2.65\,10^{-6}$	$7.16\,10^{-10}$	$3.37\,10^{3}$						
313	1.71	$6.88\,10^{-6}$	$5.36\,10^{-10}$	$1.17\,10^{4}$						
358	1.58	$1.84\,10^{-5}$	$4.14\,10^{-10}$	$4.07\,10^{4}$	$3.63\,10^{-5}$	$7.38\,10^{-9}$	$4.48\,10^{3}$			
408	1.47	$4.09\,10^{-5}$	$3.45\,10^{-10}$	$1.08\,10^{5}$	$6.63\,10^{-5}$	$3.80\,10^{-9}$	$1.59\,10^{4}$			
455	1.37	$8.57\,10^{-5}$	$2.88\,10^{-10}$	$2.71\,10^{5}$	$1.13\,10^{-4}$	$2.80\,10^{-9}$	$3.69\,10^{4}$	$1.68\,10^{-5}$	$1.09\,10^{-5}$	1.41
498	1.30	$2.09\,10^{-4}$	$2.68\,10^{-10}$	$7.11\,10^{5}$	$1.75\,10^{-4}$	$1.41\,10^{-9}$	$1.13\,10^{5}$	$3.62\,10^{-5}$	$8.50\,10^{-6}$	3.88

YSZ-8/$NaNb_{0.9}Ti_{0.1}O_{2.95}$/YSZ-8

		HF			MF			MF			LF		
T (°C)	1000/T (1/K)	σ (S.cm^{-1})	C_{eq} (F)	f_{relax} (Hz)	σ_1 (S.cm^{-1})	C_{eq1} (F)	f_{relax1} (Hz)	σ_2 (S.cm^{-1})	C_{eq2} (F)	f_{relax2} (Hz)	σ (S.cm^{-1})	C_{eq} (F)	f_{relax} (Hz)
240	1.95	$1.37\,10^{-6}$	$8.05\,10^{-11}$	$9.47\,10^{3}$	$4.20\,10^{-7}$	$1.06\,10^{-9}$	$2.99\,10^{2}$	$5.17\,10^{-7}$	$7.90\,10^{-9}$	$4.92\,10^{1}$			
288	1.78	$8.02\,10^{-6}$	$8.88\,10^{-11}$	$5.03\,10^{4}$	$2.42\,10^{-6}$	$1.22\,10^{-9}$	$1.49\,10^{3}$	$2.96\,10^{-6}$	$1.08\,10^{-8}$	$2.05\,10^{2}$			
336	1.64	$4.33\,10^{-5}$	$1.16\,10^{-10}$	$2.08\,10^{5}$	$1.24\,10^{-5}$	$1.04\,10^{-9}$	$8.90\,10^{3}$	$8.50\,10^{-6}$	$7.68\,10^{-9}$	$8.32\,10^{2}$	$7.15\,10^{-6}$	$3.09\,10^{-5}$	$7.40\,10^{-2}$
384	1.52	$2.23\,10^{-4}$	$4.34\,10^{-11}$	$2.86\,10^{6}$	$3.32\,10^{-5}$	$4.73\,10^{-10}$	$5.27\,10^{4}$	$2.08\,10^{-5}$	$5.75\,10^{-9}$	$2.72\,10^{3}$	$4.49\,10^{-5}$	$4.48\,10^{-5}$	$3.20\,10^{-1}$
435	1.41				$9.27\,10^{-5}$	$3.91\,10^{-10}$	$1.78\,10^{5}$	$5.22\,10^{-5}$	$4.39\,10^{-9}$	$8.94\,10^{3}$	$1.71\,10^{-4}$	$3.68\,10^{-5}$	1.49
484	1.32				$2.43\,10^{-4}$	$5.45\,10^{-10}$	$3.35\,10^{5}$	$1.30\,10^{-4}$	$4.10\,10^{-9}$	$2.39\,10^{4}$	$4.60\,10^{-4}$	$2.49\,10^{-5}$	5.92
534	1.24				$5.52\,10^{-4}$	$2.90\,10^{-10}$	$1.43\,10^{6}$	$2.74\,10^{-4}$	$3.29\,10^{-9}$	$6.28\,10^{4}$	$5.70\,10^{-4}$	$2.60\,10^{-5}$	7.02